GNSS Multipath Mitigation using High-Frequency Antenna Motion

Tunc Ertan, Mark L. Psiaki, Brady W. O'Hanlon, Richard A. Merluzzi and Steven P. Powell,
Cornell University, Ithaca, NY

BIOGRAPHIES

Tunc Ertan is pursuing a Ph.D. in the Sibley School of Mechanical and Aerospace Engineering at Cornell University. He received his B.S. in Mechanical Engineering from Cornell University. His current research interests are in the areas of GNSS technologies, and nonlinear estimation and filtering.

Mark L. Psiaki is a Professor of Mechanical and Aerospace Engineering. He received a B.A. in Physics and M.A. and Ph.D. degrees in Mechanical and Aerospace Engineering from Princeton University. His research interests are in the areas of GNSS technology and applications, spacecraft attitude and orbit determination, and general estimation, filtering, and detection.

Brady W. O'Hanlon is a graduate student in the School of Electrical and Computer Engineering. He received a B.S. in Electrical and Computer Engineering from Cornell University. His interests are in the areas of GNSS technology and applications, GNSS security, and space weather.

Richard A. Merluzzi is an analyst at the Johns Hopkins Applied Physics Laboratory, working in the field of ballistic missile defense. He received a B.S. degree in Engineering Physics and a Master of Engineering degree in Aerospace Engineering from Cornell University. His interests include control theory and physics-based system modeling and simulation with a focus toward guidance, navigation, and control of space vehicles.

Steven P. Powell is a Senior Engineer with the GPS and Ionospheric Studies Research Group in the Department of Electrical and Computer Engineering at Cornell University. He has M.S. and B.S. degrees in Electrical Engineering from Cornell University. He has been involved with the design, fabrication, testing, and launch activities of many scientific experiments that have flown on high altitude balloons, sounding rockets, and small satellites. He has designed ground-based and space-based custom GPS receiving systems primarily for scientific applications.

ABSTRACT

A method is developed for characterizing and compensating GNSS multipath by considering signal amplitude and phase variations in response to antenna motion. This method seeks to improve multipath rejection capabilities beyond those provided by choke-ring or other antenna technologies or by multi-correlator signal processing. A known antenna motion profile is combined with a modified multi-correlator discriminator in order to better characterize the multipath components and better isolate the direct-path component from the multipath components. It uses a batch filter to estimate the code phase, carrier phase, and amplitude of the direct signal, the relative code phase, carrier phase, carrier Doppler shift, and amplitude of each significant multipath component, and the direction of arrival of the direct and multipath components. The batch estimator solves a weighted nonlinear least-squares problem that involves mathematical models for the in-phase and quadrature accumulations over a span of sample times and a range of code-phase offsets. The batch estimator includes implicit high-pass filtering so that its results are not affected by low-frequency phase variations that might be caused by satellite motion and receiver clock drift. Experimental test results are presented based on data from an antenna articulation system operated outdoors in Ithaca, NY. Measurable improvements are observed in resulting estimates of carrier amplitude in all cases, of direct-path carrier-phase in many cases, and of direct-path code phase in some cases. Anomalous results have also been obtained, including multipath component estimates that sometimes occur in doublets that have high carrier amplitude, direction and code phase estimates that are nearly identical, and carrier phases that cause them nearly to cancel. These are believed to be the result of diffuse multipath, which is not modeled in the present study.

INTRODUCTION

Reflected multipath signals distort the in-phase (I) and quadrature (Q) accumulations within a typical GPS space-weather monitor. These distortions cause errors in the measured carrier phase and code phase. Much work has been done to try to mitigate the effects of multipath, e.g.,

Preprint from ION GNSS+ 2013

see Refs. 1, 2, 3, 4, 5 and 6. The present effort seeks to expand on the ideal of the Multipath-Estimating Delay-Lock Loop (MEDLL), as described in Refs. 1, 3, and 6.

An example of multipath distortion of a receiver's I and Q accumulations is depicted in Fig. 1. This 3-D figure plots in-phase accumulations I and quadrature accumulations Q on two orthogonal axes vs. code delay offset on the third axis. The projected view in the figure shows what is effectively a combination of I and Q, as caused by rotation about the code offset axis, vs. code offset. As expected, it looks fairly similar to what a PRN code correlation function would look like after accounting for its distortion by the receivers RF front-end filter.

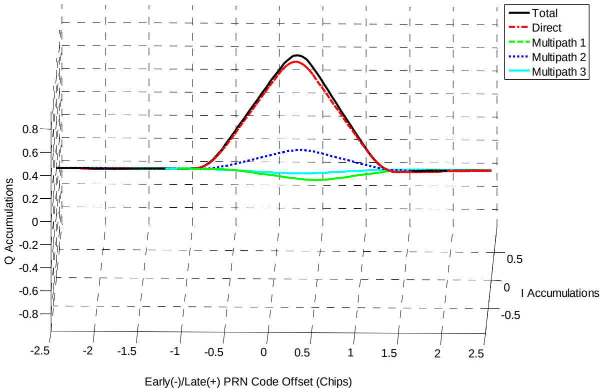

Fig. 1. Received in-phase and quadrature accumulations vs. code-offset delay relative to prompt, a 3D view.

If there were no multipath signals, then the red direct-signal curve represents what the receiver would see and use to deduce a code phase observable based on the early/late code offset timing of the peak. Unfortunately, the green, blue, and cyan multipath signals distort the total received signal to yield the black signal. The receiver is likely to measure on the black curve an absolute code phase that is biased 0.0054 chips (5.3 nsec/1.6 m/9.7 TECU) later than the true code phase. This is a relatively benign situation for the receiver whose distorted PRN code correlations are shown in Fig. 1. The error can be much larger in less benign situations.

Standard multipath mitigation strategies attempt to fit the distorted black curve to a sum of curves such as the red, green, blue, and cyan curves in Fig. 1. This fit occurs for the complex in-phase and quadrature time history depicted in Fig. 1. Each received component has a correlation peak location along the horizontal code-offset axis, but it also has a phase offset in rotation about this axis. These phase offsets are not easy to visualize in Fig. 1 due to the choice of viewing angle of this 3D plot.

Fig. 2 presents a different viewing angle of the same scenario. On this alternate figure, it is obvious that the black totaled curve and the green and cyan multipath curves have significantly different phases than the red direct-signal curve. The multipath mitigation techniques like those in Refs. 1, 3, and 6 recognize the possibility of such phase offsets and account for them in curve fitting algorithms. The goal of such algorithms is to estimate the most likely combination of true direct-signal red curve and green, blue, and cyan multipath curves that best add up to the distorted black curve. These techniques also can reduce the multipath distortion of carrier phase, which is illustrated in Fig. 2 by the phase rotation between the distorted black curve and the red true direct-signal curve, but only if there is sufficient code delay between the direct signal and the multipath components.

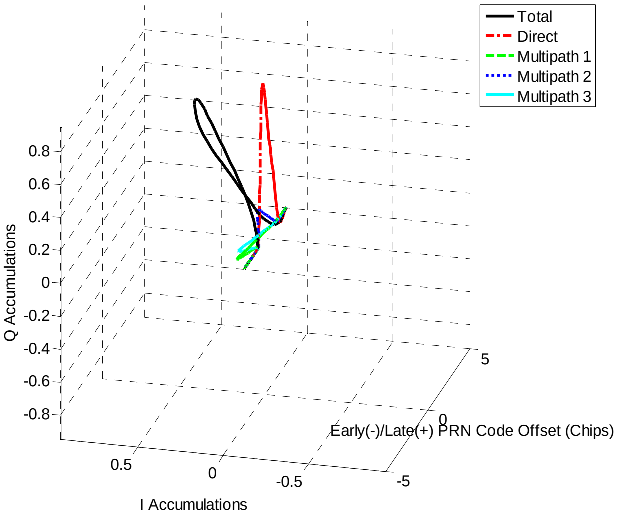

Fig. 2 Re-oriented 3D view of received in-phase and quadrature accumulations vs. code-offset.

The main new idea of the present work is to exploit the fact that the relative phases of the direct and multipath signals in Fig. 2 are strongly dependent on the antenna location. If one moves the antenna just 10 cm in a particular direction, which is about half a wavelength of the GPS L1 carrier signal, then the relative phasings of the signals in Fig. 2 morph into the situation shown in Fig. 3. The dramatic phase changes are caused by the projection of the antenna movement onto the LOS directions of the different signal components. The relative phases change between Fig. 2 and Fig. 3 due to the differing directions of arrival of the different components. Consider, for example, the phase relationship of the red direct curve and the cyan 3rd multipath component. The cyan curve is rotated counter-clockwise in phase relative to the red curve by about 120 deg. in Fig. 2. In Fig. 3, however, it is rotated about 45 deg. clockwise from the red curve. Notice, also, how there is a significant carrier-phase discrepancy between the red true signal and the black total received signal in Fig. 2. In Fig. 3 this phase offset has largely vanished.

As an experimental confirmation of this analysis, consider the actual received signal amplitude time histories depicted in Fig. 4. These data were recorded from multiple channels of a GPS receiver which was connected to a roof-mounted antenna that underwent decaying 1-dimensional sinusoidal oscillations at the end of a flexible cantilevered beam. The initial oscillation amplitude was about 13 cm peak-to-peak, and it was initiated at time t = -29 sec as measured along the figure's horizontal axis. The antenna oscillation frequency was about 2 Hz. These oscillations produced corresponding signal amplitude oscillations at this same frequency in various of the channels, most notable, the yellow (PRN 25), black (PRN 22), red (PRN 14), and solid blue (PRN 12) channels. The plotted quantities in Fig. 4 are essentially the peak amplitudes of the black correlation curves in Figs. 1-3 as they vary with antenna location. For some of the signals, this peak amplitude changes dramatically because the oscillations cause relative phase differences between the direct and multipath components that cause, alternately, constructive and destructive interference between their correlation peaks. Signals without much amplitude oscillation correspond to one of two conditions: They may have very little multipath. Alternatively, their true-signal directions of arrival and their multipath-signal directions may have nearly identical dot products with the direction of the 1D antenna oscillation in this particular experiment.

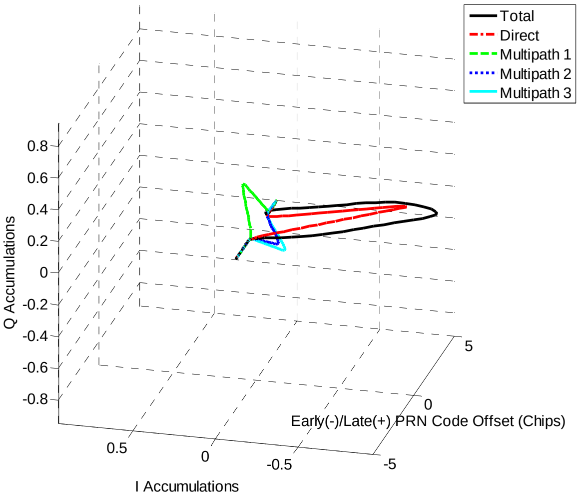

Fig. 3 Received in-phase and quadrature accumulations vs. code-offset delay at an antenna location displaced by about half a wavelength from the location corresponding to Figs 1 and 2

As confirmation that the oscillations in Fig. 4 were caused by multipath, the same test was run in an anechoic chamber in which GPS signals from a roof-mounted antenna were re-radiated. No such amplitude oscillations were observed on the anechoic chamber data.

This paper makes four contributions to the problem of multipath mitigation. First, it presents a mathematical model of the multipath effects of antenna motion. This represents a generalization of the model used to design MEDLL algorithms. Second, it develops a nonlinear batch estimator based on this mathematical model. This algorithm estimates various direct-signal and multipath-signal parameters, including relative delays, relative carrier phases, and the directions of arrival of each signal. The batch estimator constitutes, in effect, a sort of prototype discriminator for a combined multipath-estimating DLL and PLL. Third, this paper confirms the observability of the parameters of its model by considering the local uniqueness of its optimal solutions. Fourth, it applies the new batch estimator/discriminator to experimental data, and it uses the results to evaluate its effectiveness.

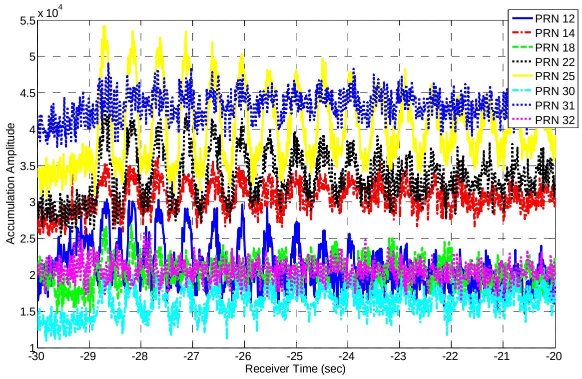

Fig. 4 Oscillatory amplitude time histories of correlation peaks as received by a spring-mounted antenna undergoing decaying 1-dimensional oscillations.

This paper's contributions are contained in 4 main sections plus conclusions. Section II defines the multipath accumulation measurement model that includes the effects of antenna motion. Section III develops a best estimator that operates on many samples of the measurement model of Section II in order to estimate parameters of the direct and multipath signals. In effect, this estimator constitutes a code-phase and carrier-phase discriminator for a coupled multipath estimating DLL/PLL. Section III also analyzes the system's observability. Section IV explains the experimental set-up and data collection campaign, and it discusses the data preprocessing that had to be carried out before the estimator of Section III could be applied to the data. Section V presents and analyzes the experimental results. Section VI summarizes the paper's contributions and gives its conclusions.

II. MEASUREMENT MODEL

The present multipath mitigation approach relies on models of the direct and multipath signal components. These models are initially defined at the raw signal level. They are then propagated through the recipes for a GNSS receiver's standard in-phase and quadrature accumulations. The result is a set of formulas for how the accumulations depend on the parameters that characterize the direct-path and multipath signals. These formulas constitute the measurement models used in the batch nonlinear estimator of Section III.

The model for the received signal from a given GPS satellite takes the form:

$$
\begin{aligned}
y_i = {} & A\cos[\omega_{IF}t_i + \phi_{NBC}(t_i)]\times \\
& \Big\{\cos[\frac{-2\pi\hat{\mathbf{r}}_0^T\mathbf{r}_a(t_i)}{\lambda}]Z_{fI}[t_i - \frac{\hat{\mathbf{r}}_0^T\mathbf{r}_a(t_i)}{c}] \\
& \quad + \sin[\frac{-2\pi\hat{\mathbf{r}}_0^T\mathbf{r}_a(t_i)}{\lambda}]Z_{fQ}[t_i - \frac{\hat{\mathbf{r}}_0^T\mathbf{r}_a(t_i)}{c}] \\
& + \sum_{m=1}^{M}\alpha_m[\cos(\Delta\phi_{\alpha m}+\Delta\omega_{\alpha m}\{t_i-\bar{t}\}-\frac{2\pi\hat{\mathbf{r}}_{\alpha m}^T\mathbf{r}_a\{t_i\}}{\lambda})\times \\
& \qquad Z_{fI}(t_i - \delta\tau_{\alpha m} - \frac{\hat{\mathbf{r}}_{\alpha m}^T\mathbf{r}_a\{t_i\}}{c}) \\
& + \sin(\Delta\phi_{\alpha m}+\Delta\omega_{\alpha m}\{t_i-\bar{t}\}-\frac{2\pi\hat{\mathbf{r}}_{\alpha m}^T\mathbf{r}_a\{t_i\}}{\lambda})\times \\
& \qquad Z_{fQ}(t_i - \delta\tau_{\alpha m} - \frac{\hat{\mathbf{r}}_{\alpha m}^T\mathbf{r}_a\{t_i\}}{c})]\Big\} \\
& + A\sin[\omega_{IF}t_i + \phi_{NBC}(t_i)]\times \\
& \Big\{-\sin[\frac{-2\pi\hat{\mathbf{r}}_0^T\mathbf{r}_a(t_i)}{\lambda}]Z_{fI}[t_i - \frac{\hat{\mathbf{r}}_0^T\mathbf{r}_a(t_i)}{c}] \\
& \quad + \cos[\frac{-2\pi\hat{\mathbf{r}}_0^T\mathbf{r}_a(t_i)}{\lambda}]Z_{fQ}[t_i - \frac{\hat{\mathbf{r}}_0^T\mathbf{r}_a(t_i)}{c}] \\
& + \sum_{m=1}^{M}\alpha_m[-\sin(\Delta\phi_{\alpha m}+\Delta\omega_{\alpha m}\{t_i-\bar{t}\}-\frac{2\pi\hat{\mathbf{r}}_{\alpha m}^T\mathbf{r}_a\{t_i\}}{\lambda})\times \\
& \qquad Z_{fI}(t_i - \delta\tau_{\alpha m} - \frac{\hat{\mathbf{r}}_{\alpha m}^T\mathbf{r}_a\{t_i\}}{c}) \\
& + \cos(\Delta\phi_{\alpha m}+\Delta\omega_{\alpha m}\{t_i-\bar{t}\}-\frac{2\pi\hat{\mathbf{r}}_{\alpha m}^T\mathbf{r}_a\{t_i\}}{\lambda})\times \\
& \qquad Z_{fQ}(t_i - \delta\tau_{\alpha m} - \frac{\hat{\mathbf{r}}_{\alpha m}^T\mathbf{r}_a\{t_i\}}{c})]\Big\} + \nu_i
\end{aligned}
\tag{1}
$$

where y_i is the raw RF front-end output sample at receiver sample time t_i. The quantity A would be the carrier amplitude at the output of the RF front-end if there were infinite RF filter bandwidth and if there were no multipath.

The constants ω_{IF}, λ, and c are, respectively the nominal intermediate frequency to which the nominal GPS carrier frequency, L1 or L2, gets mixed by the RF front-end, the nominal wavelength of the nominal GPS carrier frequency, and the speed of light in vacuum. The time history $\phi_{NBC}(t)$ is what the received negative beat carrier phase of the direct signal would have been had there been no antenna motion; it is the time integral of the received carrier Doppler shift. It is termed "negative" because it has the opposite sign to the usual beat carrier phase definition in the GPS literature. The functions $Z_{fI}(t)$ and $Z_{fQ}(t)$ are, respectively, the real (i.e., in-phase) and imaginary (i.e., quadrature) components of the signal's PRN code after it passes through the RF front-end's bandpass filter. An envelope of this filter's complex impulse response function, as in Ref. 7, can be used to compute these functions from the original wideband PRN code. The four quantities α_m, $\Delta\phi_{\alpha m}$, $\Delta\omega_{\alpha m}$, and $\delta\tau_{\alpha m}$ characterize the mth multipath component of the received signal, with α_m being its relative equivalent wideband carrier amplitude, measured relative to the direct signal A, with $\Delta\phi_{\alpha m}$ being its phase perturbation relative to the direct signal under the assumption of no antenna motion at reference time $\bar{t}$, with $\Delta\omega_{\alpha m}$ being its relative carrier Doppler shift, and with $\delta\tau_{\alpha m}$ being its delay relative to the direct signal under the assumption of no antenna motion. Typically $0 \leq \alpha_m \leq 1$ and $0 < \delta\tau_{\alpha m}$ are valid.

The 3-by-1 unit direction vector $\hat{\mathbf{r}}_0$ is the direction of the direct-signal line-of-sight ray path from the satellite to the nominal antenna location, and the 3-by-1 unit direction vector $\hat{\mathbf{r}}_{\alpha m}$ is the apparent direction vector of the direction from which the mth multipath component is arriving. Both of these direction vectors are defined in any convenient local body-fixed coordinate system. The 3-by-1 vector time history $\mathbf{r}_a(t)$ is the known antenna motion time history, in meters units and given in the same local body-fixed coordinate system as is used to define $\hat{\mathbf{r}}_0$ and each $\hat{\mathbf{r}}_{\alpha m}$. The $\mathbf{r}_a(t)$ antenna motion time history is deliberately designed to aid in multipath estimation. There a total of M multipath components in this model. The final term in Eq. (1), ν_i, is the receiver thermal noise in the ith sample.

The raw RF front-end samples are used in a receiver to compute in-phase and quadrature accumulations according to the following recipes:

$$
\begin{aligned}
I_k(\eta) = {} & \\
& \sum_{i=i_k}^{i_k+N_k-1} y_i Z_{nom}[(t_i - \tau_{DLLk} - \eta)(1+\omega_{PLLk}/\omega_c)]\times \\
& \qquad cos[\omega_{IF}t_i + \phi_{PLLk} + \omega_{PLLk}(t_i - \tau_{DLLk})]
\end{aligned}
\tag{2a}
$$

$$
\begin{aligned}
Q_k(\eta) = {} & \\
& \sum_{i=i_k}^{i_k+N_k-1} y_i Z_{nom}[(t_i - \tau_{DLLk} - \eta)(1+\omega_{PLLk}/\omega_c)]\times \\
& \qquad sin[\omega_{IF}t_i + \phi_{PLLk} + \omega_{PLLk}(t_i - \tau_{DLLk})]
\end{aligned}
\tag{2b}
$$

for the k^{th} accumulation interval, which starts at receiver time τ_{DLLk} and ends at τ_{DLLk+1}. The Doppler-shifted wide-band PRN code replica is $Z(t) = Z_{nom}[t(1+\omega_{PLLk}/\omega_c)]$, where $Z_{nom}(t)$ is the known nominal PRN code with no code Doppler shift, ω_{PLLk} is the PLL's carrier Doppler shift estimate for this interval, and ω_c is the nominal broadcast carrier frequency, i.e., $\omega_{L1} = 2\pi\text{x}1575.42\text{x}10^6$ rad/sec at L1 or $\omega_{L2} = 2\pi\text{x}1227.6\text{x}10^6$ rad/sec at L2. The two times τ_{DLLk} and τ_{DLLk+1} must be chosen by the DLL, and $Z(t)$ must be synchronized by the DLL so that $Z(t - \tau_{DLLk})$ is the prompt PRN code replica during this interval. The sample index i_k is the first sample i such that $\tau_{DLLk} \leq t_i$. The quantity N_k is the total number of samples in the interval so that the terminal index i_k+N_k-1 is the largest value of i for which $t_i < \tau_{DLLk+1}$. The phase ϕ_{PLLk} is the estimated negative beat carrier phase at the start time τ_{DLLk}. The input argument η is the shift of the PRN code replica relative to the prompt code, in seconds. A positive value of η corresponds to a PRN code replica in Eqs. (2a) and (2b) that lags behind the prompt replica.

The accumulation recipes in Eqs. (2a) and (2b) can be combined with the signal model in Eq. (1) in order to produce the following models of the computed accumulations:

$$
\begin{aligned}
I_k(\eta) = X_d\Big\{&\cos[\Delta\omega_{nom}(\bar{\tau}_k-\bar{t})+\frac{\Delta\gamma_{nom}}{2}(\bar{\tau}_k-\bar{t})^2 \\
&+\frac{2\pi\hat{\mathbf{r}}_0^T\mathbf{r}_a(\bar{\tau}_k)}{\lambda}]\times \\
&C_{ZfZI}[\eta+\Delta\tau_d-\frac{\hat{\mathbf{r}}_0^T\mathbf{r}_a(\bar{\tau}_k)}{c}] \\
&-\sin[\Delta\omega_{nom}(\bar{\tau}_k-\bar{t})+\frac{\Delta\gamma_{nom}}{2}(\bar{\tau}_k-\bar{t})^2 \\
&+\frac{2\pi\hat{\mathbf{r}}_0^T\mathbf{r}_a(\bar{\tau}_k)}{\lambda}]\times \\
&C_{ZfZQ}[\eta+\Delta\tau_d-\frac{\hat{\mathbf{r}}_0^T\mathbf{r}_a(\bar{\tau}_k)}{c}]\Big\} \\
+Y_d\Big\{&-\sin[\Delta\omega_{nom}(\bar{\tau}_k-\bar{t})+\frac{\Delta\gamma_{nom}}{2}(\bar{\tau}_k-\bar{t})^2 \\
&+\frac{2\pi\hat{\mathbf{r}}_0^T\mathbf{r}_a(\bar{\tau}_k)}{\lambda}]\times \\
&C_{ZfZI}[\eta+\Delta\tau_d-\frac{\hat{\mathbf{r}}_0^T\mathbf{r}_a(\bar{\tau}_k)}{c}] \\
&-\cos[\Delta\omega_{nom}(\bar{\tau}_k-\bar{t})+\frac{\Delta\gamma_{nom}}{2}(\bar{\tau}_k-\bar{t})^2 \\
&+\frac{2\pi\hat{\mathbf{r}}_0^T\mathbf{r}_a(\bar{\tau}_k)}{\lambda}]\times \\
&C_{ZfZQ}[\eta+\Delta\tau_d-\frac{\hat{\mathbf{r}}_0^T\mathbf{r}_a(\bar{\tau}_k)}{c}]\Big\} \\
+\sum_{m=1}^{M}\Big(X_{\alpha m}\Big\{&\cos[(\Delta\omega_{nom}+\Delta\omega_{\alpha m})(\bar{\tau}_k-\bar{t}) \\
&+\frac{\Delta\gamma_{nom}}{2}(\bar{\tau}_k-\bar{t})^2+\frac{2\pi\hat{\mathbf{r}}_{\alpha m}^T\mathbf{r}_a(\bar{\tau}_k)}{\lambda}]\times \\
&C_{ZfZI}[\eta+\Delta\tau_d-\delta\tau_{\alpha m}-\frac{\hat{\mathbf{r}}_{\alpha m}^T\mathbf{r}_a(\bar{\tau}_k)}{c}] \\
&-\sin[(\Delta\omega_{nom}+\Delta\omega_{\alpha m})(\bar{\tau}_k-\bar{t}) \\
&+\frac{\Delta\gamma_{nom}}{2}(\bar{\tau}_k-\bar{t})^2+\frac{2\pi\hat{\mathbf{r}}_{\alpha m}^T\mathbf{r}_a(\bar{\tau}_k)}{\lambda}]\times \\
&C_{ZfZQ}[\eta+\Delta\tau_d-\delta\tau_{\alpha m}-\frac{\hat{\mathbf{r}}_{\alpha m}^T\mathbf{r}_a(\bar{\tau}_k)}{c}]\Big\} \\
+Y_{\alpha m}\Big\{&-\sin[(\Delta\omega_{nom}+\Delta\omega_{\alpha m})(\bar{\tau}_k-\bar{t}) \\
&+\frac{\Delta\gamma_{nom}}{2}(\bar{\tau}_k-\bar{t})^2+\frac{2\pi\hat{\mathbf{r}}_{\alpha m}^T\mathbf{r}_a(\bar{\tau}_k)}{\lambda}]\times \\
&C_{ZfZI}[\eta+\Delta\tau_d-\delta\tau_{\alpha m}-\frac{\hat{\mathbf{r}}_{\alpha m}^T\mathbf{r}_a(\bar{\tau}_k)}{c}] \\
&-\cos[(\Delta\omega_{nom}+\Delta\omega_{\alpha m})(\bar{\tau}_k-\bar{t}) \\
&+\frac{\Delta\gamma_{nom}}{2}(\bar{\tau}_k-\bar{t})^2+\frac{2\pi\hat{\mathbf{r}}_{\alpha m}^T\mathbf{r}_a(\bar{\tau}_k)}{\lambda}]\times \\
&C_{ZfZQ}[\eta+\Delta\tau_d-\delta\tau_{\alpha m}-\frac{\hat{\mathbf{r}}_{\alpha m}^T\mathbf{r}_a(\bar{\tau}_k)}{c}]\Big\}\Big) \\
+\ & n_{Ik}(\eta)
\end{aligned}
\tag{3a}
$$

$$
\begin{aligned}
Q_k(\eta) = X_d\Big\{&\sin[\Delta\omega_{nom}(\bar{\tau}_k-\bar{t})+\frac{\Delta\gamma_{nom}}{2}(\bar{\tau}_k-\bar{t})^2 \\
&+\frac{2\pi\hat{\mathbf{r}}_0^T\mathbf{r}_a(\bar{\tau}_k)}{\lambda}]\times \\
&C_{ZfZI}[\eta+\Delta\tau_d-\frac{\hat{\mathbf{r}}_0^T\mathbf{r}_a(\bar{\tau}_k)}{c}] \\
&+\cos[\Delta\omega_{nom}(\bar{\tau}_k-\bar{t})+\frac{\Delta\gamma_{nom}}{2}(\bar{\tau}_k-\bar{t})^2 \\
&+\frac{2\pi\hat{\mathbf{r}}_0^T\mathbf{r}_a(\bar{\tau}_k)}{\lambda}]\times \\
&C_{ZfZQ}[\eta+\Delta\tau_d-\frac{\hat{\mathbf{r}}_0^T\mathbf{r}_a(\bar{\tau}_k)}{c}]\Big\} \\
+Y_d\Big\{&\cos[\Delta\omega_{nom}(\bar{\tau}_k-\bar{t})+\frac{\Delta\gamma_{nom}}{2}(\bar{\tau}_k-\bar{t})^2 \\
&+\frac{2\pi\hat{\mathbf{r}}_0^T\mathbf{r}_a(\bar{\tau}_k)}{\lambda}]\times \\
&C_{ZfZI}[\eta+\Delta\tau_d-\frac{\hat{\mathbf{r}}_0^T\mathbf{r}_a(\bar{\tau}_k)}{c}] \\
&-\sin[\Delta\omega_{nom}(\bar{\tau}_k-\bar{t})+\frac{\Delta\gamma_{nom}}{2}(\bar{\tau}_k-\bar{t})^2
\end{aligned}
$$

$$
\begin{aligned}
&\qquad +\frac{2\pi\hat{\mathbf{r}}_0^T\,\mathbf{r}_a(\bar{\tau}_k)}{\lambda}]\times\\
&\quad C_{ZfZQ}[\eta+\Delta\tau_d-\frac{\hat{\mathbf{r}}_0^T\,\mathbf{r}_a(\bar{\tau}_k)}{c}]\}\\
&+\sum_{m=1}^{M}\Big(X_{\alpha m}\{\sin[(\Delta\omega_{nom}+\Delta\omega_{\alpha m})(\bar{\tau}_k-\bar{t})\\
&\qquad +\frac{\Delta\gamma_{nom}}{2}(\bar{\tau}_k-\bar{t})^2+\frac{2\pi\hat{\mathbf{r}}_{\alpha m}^T\mathbf{r}_a(\bar{\tau}_k)}{\lambda}]\times\\
&\quad C_{ZfZI}[\eta+\Delta\tau_d-\delta\tau_{\alpha m}-\frac{\hat{\mathbf{r}}_{\alpha m}^T\mathbf{r}_a(\bar{\tau}_k)}{c}]\\
&\quad +\cos[(\Delta\omega_{nom}+\Delta\omega_{\alpha m})(\bar{\tau}_k-\bar{t})\\
&\qquad +\frac{\Delta\gamma_{nom}}{2}(\bar{\tau}_k-\bar{t})^2+\frac{2\pi\hat{\mathbf{r}}_{\alpha m}^T\mathbf{r}_a(\bar{\tau}_k)}{\lambda}]\times\\
&\quad C_{ZfZQ}[\eta+\Delta\tau_d-\delta\tau_{\alpha m}-\frac{\hat{\mathbf{r}}_{\alpha m}^T\mathbf{r}_a(\bar{\tau}_k)}{c}]\}\\
&\quad +Y_{\alpha m}\{\cos[(\Delta\omega_{nom}+\Delta\omega_{\alpha m})(\bar{\tau}_k-\bar{t})\\
&\qquad +\frac{\Delta\gamma_{nom}}{2}(\bar{\tau}_k-\bar{t})^2+\frac{2\pi\hat{\mathbf{r}}_{\alpha m}^T\mathbf{r}_a(\bar{\tau}_k)}{\lambda}]\times\\
&\quad C_{ZfZI}[\eta+\Delta\tau_d-\delta\tau_{\alpha m}-\frac{\hat{\mathbf{r}}_{\alpha m}^T\mathbf{r}_a(\bar{\tau}_k)}{c}]\\
&\quad -\sin[(\Delta\omega_{nom}+\Delta\omega_{\alpha m})(\bar{\tau}_k-\bar{t})\\
&\qquad +\frac{\Delta\gamma_{nom}}{2}(\bar{\tau}_k-\bar{t})^2+\frac{2\pi\hat{\mathbf{r}}_{\alpha m}^T\mathbf{r}_a(\bar{\tau}_k)}{\lambda}]\times\\
&\quad C_{ZfZQ}[\eta+\Delta\tau_d-\delta\tau_{\alpha m}-\frac{\hat{\mathbf{r}}_{\alpha m}^T\mathbf{r}_a(\bar{\tau}_k)}{c}]\}\Big)\\
&+\ n_{Qk}(\eta)
\end{aligned}
\tag{3b}
$$

The following definitions hold for the many new quantities used in Eqs. (3a) and (3b):

$$X_d=\frac{A\bar{N}}{2}\cos(\Delta\phi_d) \tag{4a}$$

$$Y_d=\frac{A\bar{N}}{2}\sin(\Delta\phi_d) \tag{4b}$$

are the in-phase and quadrature phasor components of the direct signal, with $\bar{N}$ being the mean number of samples in an accumulation, i.e., the mean value of N_k, and with $\Delta\phi_d$ being the difference between the negative beat carrier phase replica used in the accumulations calculations and the true negative beat carrier phase of the direct signal at the nominal midpoint time of all the accumulation intervals under consideration, $\bar{t}$:

$$\Delta\phi_d\cong\phi_{PLLk_{\mathrm{mod}}}+\omega_{PLLk}(\bar{t}-\tau_{DLLk_{\mathrm{mod}}})-\phi_{NBC}(\bar{t}) \tag{5}$$

with k_{mid} being the index of the accumulation interval that encompasses $\bar{t}$:

$$\tau_{DLLk_{mid}}\le\bar{t}<\tau_{DLL(k_{mid}+1)} \tag{6}$$

The models in Eqs. (3a) and (3b) include the multipath phasors

$$X_{\alpha m}=\frac{A\bar{N}}{2}\alpha_m\cos(\Delta\phi_d-\Delta\phi_{\alpha m})\quad\text{for } m=\ 1, ..., M \tag{7a}$$

$$Y_{\alpha m}=\frac{A\bar{N}}{2}\alpha_m\sin(\Delta\phi_d-\Delta\phi_{\alpha m})\quad\text{for } m=\ 1, ..., M \tag{7b}$$

The quantities $\Delta\omega_{nom}$ and $\Delta\gamma_{nom}$ are, respectively, the carrier Doppler shift residual error between the PLL NCO and the direct signal at time t_{nom} and the carrier Doppler shift rate residual error for the entire interval in question. Thus, a model of the entire residual carrier-phase difference between the PLL NCO negative beat carrier phase, the one used for base-band mixing in the accumulation recipes of Eqs. (2a) and (2b), and the true received carrier phase of the direct signal, absent antenna motion effects, is

$$
\begin{aligned}
\Delta\phi_d+\Delta\omega_{nom}(t-\bar{t})+\frac{\Delta\gamma_{nom}}{2}(t-\bar{t})^2&\\
=\phi_{PLLk}+\omega_{PLLk}(t-\tau_{DLLk})-\phi_{NBC}(t)&
\end{aligned}
\tag{8}
$$

This one model is assumed to be reasonable for all accumulation intervals of interest, k = 1, ..., K. The inclusion of the unknowns X_d, Y_d, $\Delta\omega_{nom}$, and $\Delta\gamma_{nom}$ in the multipath estimation problem, when coupled with the phase model in Eq. (8), has the effect of batch high-pass filtering the phase effects on the accumulations prior to matching phase variations to antenna motions. This is a reasonable approach that deals effectively with the GNSS satellite motions, the receiver clock drift, and possible motions of the platform on which the antenna is mounted.

Note that the actions of a high bandwidth PLL might make the model in Eq. (8) invalid due to the introduction of high-frequency variations in ϕ_{PLLk} and ω_{PLLk} for different values of k in the range 1 to K. Such variations could be noise induced or they could be induced by the PLL trying to track the effects of the antenna motion. Therefore, in applying this model, a best-fit polynomial approximation of the negative beat carrier phase is used to create an effective PLL negative beat carrier phase time history over the interval k = 1, ..., K. The average phase error between this polynomial and the receiver PLL's actual phase NCO time history for each accumulation interval is then used to pre-process the corresponding $[I_k(\eta);Q_k(\eta)]$ accumulation vector by rotating it in the $[I;Q]$ plane in order to yield the accumulations that would have been computed had the NCO used the negative beat carrier phase in the polynomial model. The polynomial model is derived by performing a least-squares fit to the PLL negative beat carrier phase time history for a data interval that includes a span of time just before the $r_a(t)$ motion and another span of time just after the motion. The resulting $[I;Q]$ accumulations retain the motion effects and the high-frequency noise effects.

The time $\bar{\tau}_k$ is the mid-point of the k^{th} accumulation interval:

$$\bar{\tau}_k = \frac{1}{2}[\tau_{DLLk} + \tau_{DLLk+1}] \tag{9}$$

The $\boldsymbol{r}_a(\bar{\tau}_k)$ terms in Eqs. (3a) and (3b) presume that the antenna position stays fixed at this value during the entire k^{th} accumulation interval. Therefore, the highest frequency content in the $\boldsymbol{r}_a(t)$ time history must be significantly lower than half the accumulation frequency.

The quantity $\Delta\tau_d$ is the average code-phase error between the prompt PRN code replica used in the accumulations in Eqs. (2a) and (2b) if $\eta = 0$ and the true received direct signal:

$$\Delta\tau_d = \frac{1}{2K}\sum_{k=1}^{K}[(\tau_{DLLk} - \tau_k) + (\tau_{DLLk+1} - \tau_{k+1})] \tag{10}$$

where τ_k and τ_{k+1} are the actual times when the given segment of the true filtered version of the PRN code starts and stops at the output of the RF front-end. This given segment is the same segment as the one whose wide-band version extends from $Z(0)$ to $Z(\tau_{DLLk+1} - \tau_{DLLk})$, consistent with the definition of $Z(t)$ in the text that follows Eqs. (2a) and (2b).

The accumulation models in Eqs. (3a) and (3b) presume that this code offset would stay constant over the K accumulation intervals were it not for the effects of the $\boldsymbol{r}_a(t)$ antenna motion. In practice, this can be difficult to achieve in a severe multipath environment. Large multipath-induced changes in the $[I;Q]$ accumulations can cause large swings in the DLL's computed τ_{DLLk} and τ_{DLLk+1} values. Therefore, in order to use the accumulations model in its current form, it is necessary to use an aided DLL over the interval of antenna motion. Carrier aiding can supply the needed insensitivity to multipath if implemented properly for the interval of $\boldsymbol{r}_a(t)$ motion. In one implementation, a carrier-aided DLL has its code phase feedback term turned off during the $\boldsymbol{r}_a(t)$ motion interval. The best such approach would combine zero-code-phase-feedback during the motion interval with carrier aiding from the polynomial fit to the PLL negative beat carrier phase with fit parameters determined using data only from time spans just before and after the motion interval, as described above. This approach yields DLL code phase that does not respond to the high-frequency antenna motion, consistent with the accumulations model in Eqs. (3a) and (3b).

Note that the special PLL and DLL requirements discussed above apply only because of the batch estimation form of the accumulations model that has been derived. It would be straightforward to derive a suitable multipath model of the accumulations that did not place such unusual requirements on the PLL and the DLL. In that case, a different estimator would be needed than is developed in Section III of this paper. It is likely that a sequential estimator such as a Kalman filter, would be the appropriate choice in such a situation. The multipath model form and estimator used here have been chosen to simplify the initial development and testing of this multipath estimation concept using off-line data analysis. Further work should be carried out in order to design a practical real-time version of the present multipath estimation schemes.

The functions $C_{ZfZI}(\tau)$ and $C_{ZfZQ}(\tau)$ are, respectively, the real and imaginary components of the cross-correlation between the complex filtered PRN code $Z_{fI}(t) + jZ_{fQ}(t)$ in the received signal and the wide-band PRN code $Z(t)$ used in the accumulation recipes. These functions can be computed using a modified version of the formula in Ref. 7:

$$\begin{aligned} C_{ZfZ}(\tau) &= C_{ZfZI}(\tau) + jC_{ZfZQ}(\tau) \\ &= e^{-j\Delta\phi_f}\int_0^{t_{max}} h(t)C_{ZZ}(t - \tau - \Delta\tau_{Df})dt \end{aligned} \tag{11}$$

where the function $C_{ZZ}(\tau)$ is the known real-valued autocorrelation function of the wide-band PRN code $Z(t)$, $h(t)$ is the complex-valued envelop impulse response function of the RF front-end filter, t_{max} is the modeled finite duration of that response, $\Delta\phi_f$ is the small phase rotation caused the filter's frequency asymmetry, and $\Delta\tau_{Df}$ is the average delay through the filter. The filter parameters $\Delta\phi_f$ and $\Delta\tau_{Df}$ can be estimated from $h(t)$ by considering its effects on a single PRN code chip. The filter impulse response function can be estimated using the techniques of Ref. 7.

The receiver thermal noise terms in Eqs. (3a) and (3b) are $n_{Ik}(\eta)$ and $n_{Qk}(\eta)$. They both are zero-mean Gaussian random noise samples with variance equal to σ_{IQ}^2. The quantities $n_{Ik}(\eta_a)$ and $n_{Qk}(\eta_b)$ are uncorrelated for any accumulation offsets η_a and η_b. The following non-zero noise correlation, however, apply to each of these sequences:

$$\begin{aligned} E\{n_{Ik}(\eta_a)n_{Ik}(\eta_b)\} &= E\{n_{Qk}(\eta_a)n_{Qk}(\eta_b)\} \\ &= \sigma_{IQ}^2 C_{ZZ}(\eta_a - \eta_b) \end{aligned} \tag{12}$$

Thus, the autocorrelation of the wide-band PRN code used in the accumulation recipes of Eqs. (2a) and (2b) induces noise correlation between in-phase accumulations with different code delay offsets and between quadrature accumulations different offsets.

The accumulation models in Eqs. (3a) and (3b) can be simplified into the forms:

$$\begin{aligned} I_k(\eta) = {} & X_d \tilde{C}_{ZfZI}\{[\Delta\omega_{nom}(\bar{\tau}_k-\bar{t}) + \frac{\Delta\gamma_{nom}}{2}(\bar{\tau}_k-\bar{t})^2 \\ & + \frac{2\pi\hat{\mathbf{r}}_0^T\mathbf{r}_a(\bar{\tau}_k)}{\lambda}],[\eta+\Delta\tau_d - \frac{\hat{\mathbf{r}}_0^T\mathbf{r}_a(\bar{\tau}_k)}{c}]\} \\ & - Y_d\tilde{C}_{ZfZQ}\{[\Delta\omega_{nom}(\bar{\tau}_k-\bar{t}) + \frac{\Delta\gamma_{nom}}{2}(\bar{\tau}_k-\bar{t})^2 \\ & + \frac{2\pi\hat{\mathbf{r}}_0^T\mathbf{r}_a(\bar{\tau}_k)}{\lambda}],[\eta+\Delta\tau_d - \frac{\hat{\mathbf{r}}_0^T\mathbf{r}_a(\bar{\tau}_k)}{c}]\} \\ & + \sum_{m=1}^{M}\Big(X_{\alpha m}\tilde{C}_{ZfZI}\{[(\Delta\omega_{nom}+\Delta\omega_{\alpha m})(\bar{\tau}_k-\bar{t}) \\ & + \frac{\Delta\gamma_{nom}}{2}(\bar{\tau}_k-\bar{t})^2 + \frac{2\pi\hat{\mathbf{r}}_{\alpha m}^T\mathbf{r}_a(\bar{\tau}_k)}{\lambda}], \\ & [\eta+\Delta\tau_d-\delta\tau_{\alpha m}-\frac{\hat{\mathbf{r}}_{\alpha m}^T\mathbf{r}_a(\bar{\tau}_k)}{c}]\} \\ & - Y_{\alpha m}\tilde{C}_{ZfZQ}\{[(\Delta\omega_{nom}+\Delta\omega_{\alpha m})(\bar{\tau}_k-\bar{t}) \\ & + \frac{\Delta\gamma_{nom}}{2}(\bar{\tau}_k-\bar{t})^2 + \frac{2\pi\hat{\mathbf{r}}_{\alpha m}^T\mathbf{r}_a(\bar{\tau}_k)}{\lambda}], \\ & [\eta+\Delta\tau_d-\delta\tau_{\alpha m}-\frac{\hat{\mathbf{r}}_{\alpha m}^T\mathbf{r}_a(\bar{\tau}_k)}{c}]\}\Big) \\ & + n_{Ik}(\eta) \end{aligned} \tag{13a}$$

$$\begin{aligned} Q_k(\eta) = {} & X_d \tilde{C}_{ZfZQ}\{[\Delta\omega_{nom}(\bar{\tau}_k-\bar{t}) + \frac{\Delta\gamma_{nom}}{2}(\bar{\tau}_k-\bar{t})^2 \\ & + \frac{2\pi\hat{\mathbf{r}}_0^T\mathbf{r}_a(\bar{\tau}_k)}{\lambda}],[\eta+\Delta\tau_d - \frac{\hat{\mathbf{r}}_0^T\mathbf{r}_a(\bar{\tau}_k)}{c}]\} \\ & + Y_d\tilde{C}_{ZfZI}\{[\Delta\omega_{nom}(\bar{\tau}_k-\bar{t}) + \frac{\Delta\gamma_{nom}}{2}(\bar{\tau}_k-\bar{t})^2 \\ & + \frac{2\pi\hat{\mathbf{r}}_0^T\mathbf{r}_a(\bar{\tau}_k)}{\lambda}],[\eta+\Delta\tau_d - \frac{\hat{\mathbf{r}}_0^T\mathbf{r}_a(\bar{\tau}_k)}{c}]\} \\ & + \sum_{m=1}^{M}\Big(X_{\alpha m}\tilde{C}_{ZfZQ}\{[(\Delta\omega_{nom}+\Delta\omega_{\alpha m})(\bar{\tau}_k-\bar{t}) \\ & + \frac{\Delta\gamma_{nom}}{2}(\bar{\tau}_k-\bar{t})^2 + \frac{2\pi\hat{\mathbf{r}}_{\alpha m}^T\mathbf{r}_a(\bar{\tau}_k)}{\lambda}], \\ & [\eta+\Delta\tau_d-\delta\tau_{\alpha m}-\frac{\hat{\mathbf{r}}_{\alpha m}^T\mathbf{r}_a(\bar{\tau}_k)}{c}]\} \\ & + Y_{\alpha m}\tilde{C}_{ZfZI}\{[(\Delta\omega_{nom}+\Delta\omega_{\alpha m})(\bar{\tau}_k-\bar{t}) \\ & + \frac{\Delta\gamma_{nom}}{2}(\bar{\tau}_k-\bar{t})^2 + \frac{2\pi\hat{\mathbf{r}}_{\alpha m}^T\mathbf{r}_a(\bar{\tau}_k)}{\lambda}], \\ & [\eta+\Delta\tau_d-\delta\tau_{\alpha m}-\frac{\hat{\mathbf{r}}_{\alpha m}^T\mathbf{r}_a(\bar{\tau}_k)}{c}]\}\Big) \\ & + n_{Qk}(\eta) \end{aligned} \tag{13b}$$

where the modified 2-argument correlation/rotation functions used to develop Eqs. (13a) and (13b) from Eqs. (3a) and (3b) are defined to be

$$\tilde{C}_{ZfZI}(\phi,\tau) = \cos\phi\, C_{ZfZI}(\tau) - \sin\phi\, C_{ZfZQ}(\tau) \tag{14a}$$

$$\tilde{C}_{ZfZQ}(\phi,\tau) = \sin\phi\, C_{ZfZI}(\tau) + \cos\phi\, C_{ZfZQ}(\tau) \tag{14b}$$

A typical receiver computes $I_k(\eta)$ and $Q_k(\eta)$ accumulations at a set of code-phase offsets, η_1, η_2, η_3, ..., η_L. For example, accumulations might be computed for $L = 3$ offsets, $\eta_1 = -0.5/f_c$, $\eta_2 = 0$, and $\eta_3 = +0.5/f_c$, where $f_c = f_{cnom}[1+(\omega_{PLL}/\omega_c)]$ is the Doppler-shifted PRN code chipping rate. These would correspond, respectively to half-chip early accumulations, prompt accumulations, and half-chip late accumulations.

Compact measurement models of all the accumulations $I_k(\eta_l)$ and $Q_k(\eta_l)$ for $l = 1, ..., L$ can be developed using matrix/vector notation. This development starts by stacking the accumulations into L-dimensional accumulation measurement vectors as follows:

$$\mathbf{z}_{Ik} = \begin{bmatrix} I_k(\eta_1) \\ I_k(\eta_2) \\ I_k(\eta_3) \\ \vdots \\ I_k(\eta_L) \end{bmatrix} \quad \text{and} \quad \mathbf{z}_{Qk} = \begin{bmatrix} Q_k(\eta_1) \\ Q_k(\eta_2) \\ Q_k(\eta_3) \\ \vdots \\ Q_k(\eta_L) \end{bmatrix} \tag{15}$$

Additional useful vector definitions are the L-dimensional filtered PRN code in-phase and quadrature correlation/rotation functions

$$\mathbf{c}_I(\phi,\tau) = \begin{bmatrix} \tilde{C}_{ZfZI}(\phi,\eta_1+\tau) \\ \tilde{C}_{ZfZI}(\phi,\eta_2+\tau) \\ \tilde{C}_{ZfZI}(\phi,\eta_3+\tau) \\ \vdots \\ \tilde{C}_{ZfZI}(\phi,\eta_L+\tau) \end{bmatrix} \quad \text{and} \quad \mathbf{c}_Q(\phi,\tau) = \begin{bmatrix} \tilde{C}_{ZfZQ}(\phi,\eta_1+\tau) \\ \tilde{C}_{ZfZQ}(\phi,\eta_2+\tau) \\ \tilde{C}_{ZfZQ}(\phi,\eta_3+\tau) \\ \vdots \\ \tilde{C}_{ZfZQ}(\phi,\eta_L+\tau) \end{bmatrix} \tag{16}$$

and the L-dimensional noise vectors

$$\mathbf{n}_{Ik} = \begin{bmatrix} n_{Ik}(\eta_1) \\ n_{Ik}(\eta_2) \\ n_{Ik}(\eta_3) \\ \vdots \\ n_{Ik}(\eta_L) \end{bmatrix} \quad \text{and} \quad \mathbf{n}_{Qk} = \begin{bmatrix} n_{Qk}(\eta_1) \\ n_{Qk}(\eta_2) \\ n_{Qk}(\eta_3) \\ \vdots \\ n_{Qk}(\eta_L) \end{bmatrix} \tag{17}$$

A useful matrix is the L-by-L-dimensional measurement noise covariance matrix:

$$\begin{aligned} R_k & = E\{\mathbf{n}_{Ik}\mathbf{n}_{Ik}^{\mathrm{T}}\} = E\{\mathbf{n}_{Qk}\mathbf{n}_{Qk}^{\mathrm{T}}\} \\ & = \sigma_{IQ}^2 \begin{bmatrix} 1 & C_{ZZ}(\eta_1-\eta_2) & C_{ZZ}(\eta_1-\eta_3) & \dots & C_{ZZ}(\eta_1-\eta_L) \\ C_{ZZ}(\eta_1-\eta_2) & 1 & C_{ZZ}(\eta_2-\eta_3) & \dots & C_{ZZ}(\eta_2-\eta_L) \\ C_{ZZ}(\eta_1-\eta_3) & C_{ZZ}(\eta_2-\eta_3) & 1 & \dots & C_{ZZ}(\eta_3-\eta_L) \\ \vdots & \vdots & \vdots & \ddots & \vdots \\ C_{ZZ}(\eta_1-\eta_L) & C_{ZZ}(\eta_2-\eta_L) & C_{ZZ}(\eta_3-\eta_L) & \dots & 1 \end{bmatrix} \end{aligned} \tag{18}$$

Given the foregoing vector and matrix definitions, the L in-phase and quadrature accumulation measurements can be modeled by the following two vector equations:

$$
\begin{aligned}
\boldsymbol{z}_{Ik} = {} & \boldsymbol{c}_I\{[\Delta\omega_{nom}(\bar{\tau}_k-\bar{t}) + \frac{\Delta\gamma_{nom}}{2}(\bar{\tau}_k-\bar{t})^2 \\
& \qquad + \frac{2\pi\hat{\boldsymbol{r}}_0^T\boldsymbol{r}_a(\bar{\tau}_k)}{\lambda}],[\Delta\tau_d - \frac{\hat{\boldsymbol{r}}_0^T\boldsymbol{r}_a(\bar{\tau}_k)}{c}]\}X_d \\
& -\boldsymbol{c}_Q\{[\Delta\omega_{nom}(\bar{\tau}_k-\bar{t}) + \frac{\Delta\gamma_{nom}}{2}(\bar{\tau}_k-\bar{t})^2 \\
& \qquad + \frac{2\pi\hat{\boldsymbol{r}}_0^T\boldsymbol{r}_a(\bar{\tau}_k)}{\lambda}],[\Delta\tau_d - \frac{\hat{\boldsymbol{r}}_0^T\boldsymbol{r}_a(\bar{\tau}_k)}{c}]\}Y_d \\
& + \sum_{m=1}^{M}\Big(\boldsymbol{c}_I\{[(\Delta\omega_{nom}+\Delta\omega_{\alpha m})(\bar{\tau}_k-\bar{t}) \\
& \qquad + \frac{\Delta\gamma_{nom}}{2}(\bar{\tau}_k-\bar{t})^2 + \frac{2\pi\hat{\boldsymbol{r}}_{\alpha m}^T\boldsymbol{r}_a(\bar{\tau}_k)}{\lambda}], \\
& \qquad [\Delta\tau_d - \delta\tau_{\alpha m} - \frac{\hat{\boldsymbol{r}}_{\alpha m}^T\boldsymbol{r}_a(\bar{\tau}_k)}{c}]\}X_{\alpha m} \\
& \quad -\boldsymbol{c}_Q\{[(\Delta\omega_{nom}+\Delta\omega_{\alpha m})(\bar{\tau}_k-\bar{t}) \\
& \qquad + \frac{\Delta\gamma_{nom}}{2}(\bar{\tau}_k-\bar{t})^2 + \frac{2\pi\hat{\boldsymbol{r}}_{\alpha m}^T\boldsymbol{r}_a(\bar{\tau}_k)}{\lambda}], \\
& \qquad [\Delta\tau_d - \delta\tau_{\alpha m} - \frac{\hat{\boldsymbol{r}}_{\alpha m}^T\boldsymbol{r}_a(\bar{\tau}_k)}{c}]\}Y_{\alpha m}\Big) \\
& +\boldsymbol{n}_{Ik} \\
= {} & \boldsymbol{h}_I[\boldsymbol{x};\bar{\tau}_k,\boldsymbol{r}_a(\bar{\tau}_k)] + \boldsymbol{n}_{Ik}
\end{aligned}
\tag{19a}
$$

$$
\begin{aligned}
\boldsymbol{z}_{Qk} = {} & \boldsymbol{c}_Q\{[\Delta\omega_{nom}(\bar{\tau}_k-\bar{t}) + \frac{\Delta\gamma_{nom}}{2}(\bar{\tau}_k-\bar{t})^2 \\
& \qquad + \frac{2\pi\hat{\boldsymbol{r}}_0^T\boldsymbol{r}_a(\bar{\tau}_k)}{\lambda}],[\Delta\tau_d - \frac{\hat{\boldsymbol{r}}_0^T\boldsymbol{r}_a(\bar{\tau}_k)}{c}]\}X_d \\
& +\boldsymbol{c}_I\{[\Delta\omega_{nom}(\bar{\tau}_k-\bar{t}) + \frac{\Delta\gamma_{nom}}{2}(\bar{\tau}_k-\bar{t})^2 \\
& \qquad + \frac{2\pi\hat{\boldsymbol{r}}_0^T\boldsymbol{r}_a(\bar{\tau}_k)}{\lambda}],[\Delta\tau_d - \frac{\hat{\boldsymbol{r}}_0^T\boldsymbol{r}_a(\bar{\tau}_k)}{c}]\}Y_d \\
& + \sum_{m=1}^{M}\Big(\boldsymbol{c}_Q\{[(\Delta\omega_{nom}+\Delta\omega_{\alpha m})(\bar{\tau}_k-\bar{t}) \\
& \qquad + \frac{\Delta\gamma_{nom}}{2}(\bar{\tau}_k-\bar{t})^2 + \frac{2\pi\hat{\boldsymbol{r}}_{\alpha m}^T\boldsymbol{r}_a(\bar{\tau}_k)}{\lambda}], \\
& \qquad [\Delta\tau_d - \delta\tau_{\alpha m} - \frac{\hat{\boldsymbol{r}}_{\alpha m}^T\boldsymbol{r}_a(\bar{\tau}_k)}{c}]\}X_{\alpha m} \\
& \quad +\boldsymbol{c}_I\{[(\Delta\omega_{nom}+\Delta\omega_{\alpha m})(\bar{\tau}_k-\bar{t}) \\
& \qquad + \frac{\Delta\gamma_{nom}}{2}(\bar{\tau}_k-\bar{t})^2 + \frac{2\pi\hat{\boldsymbol{r}}_{\alpha m}^T\boldsymbol{r}_a(\bar{\tau}_k)}{\lambda}], \\
& \qquad [\Delta\tau_d - \delta\tau_{\alpha m} - \frac{\hat{\boldsymbol{r}}_{\alpha m}^T\boldsymbol{r}_a(\bar{\tau}_k)}{c}]\}Y_{\alpha m}\Big) \\
& +\boldsymbol{n}_{Qk} \\
= {} & \boldsymbol{h}_Q[\boldsymbol{x};\bar{\tau}_k,\boldsymbol{r}_a(\bar{\tau}_k)] + \boldsymbol{n}_{Qk}
\end{aligned}
\tag{19b}
$$

where the vector of unknowns that is to be estimated by the multipath estimating DLL discriminator is defined to be the following (8+7M)-dimensional vector

$$
\boldsymbol{x} = \begin{bmatrix} \Delta\omega_{nom} \\ \Delta\gamma_{nom} \\ \Delta\tau_d \\ \hat{\boldsymbol{r}}_0 \\ X_d \\ Y_d \\ \Delta\omega_{\alpha 1} \\ \delta\tau_{\alpha 1} \\ \hat{\boldsymbol{r}}_{\alpha 1} \\ X_{\alpha 1} \\ Y_{\alpha 1} \\ \vdots \\ \Delta\omega_{\alpha M} \\ \delta\tau_{\alpha M} \\ \hat{\boldsymbol{r}}_{\alpha M} \\ X_{\alpha M} \\ Y_{\alpha M} \end{bmatrix}
\tag{20}
$$

and where Eq. (19a) and (19b) serve to define the L-by-1 nonlinear measurement functions $\boldsymbol{h}_I[\boldsymbol{x};\bar{\tau}_k,\boldsymbol{r}_a(\bar{\tau}_k)]$ and $\boldsymbol{h}_Q[\boldsymbol{x};\bar{\tau}_k,\boldsymbol{r}_a(\bar{\tau}_k)]$.

III. MULTIPATH MITIGATION BATCH ESTIMATOR

This section develops a form of multipath-insensitive DLL/PLL discriminator. It does this by posing and solving an optimal batch estimation problem based on the accumulation measurement model in Eqs. (19a) and (19b).

A. Examples of Simple DLL and PLL Discriminators

Recall that a DLL discriminator provides a means of forming an estimate of $\Delta\tau_d$. One typical DLL discriminator is the non-coherent early-minus-late dot product discriminator. Given early, prompt, and late accumulations, respectively $I_k(-\Delta\eta)$, $Q_k(-\Delta\eta)$, $I_k(0)$, $Q_k(0)$, $I_k(\Delta\eta)$, and $Q_k(\Delta\eta)$, this discriminator yields the estimate

$$
\begin{aligned}
\Delta\hat{\tau}_d = {} & \{[I_k(-\Delta\eta)-I_k(\Delta\eta)]I_k(0) \\
& -[Q_k(-\Delta\eta)-Q_k(\Delta\eta)]Q_k(0)\}/\{2f_c[I_k^2(0)+Q_k^2(0)]\}
\end{aligned}
\tag{21}
$$

where the (^) overstrike on $\Delta\hat{\tau}_d$ indicates that it is an estimated quantity. This estimate is reasonable if there are no multipath effects, if the filtered PRN code correlation functions are approximately $C_{ZfZI}(t) = C_{ZZ}(t)$ and $C_{ZfZQ}(t) = 0$, i.e., if they are approximately equal to their wide-band counterparts, and if the code phase offset $\Delta\tau_d$ is not too large. This analysis also assumes that the wideband PRN code autocorrelation function is approximately equal to the triangular pulse function:

$$C_{ZZ}(\tau) = \begin{cases} 0 & \text{if } f_c\tau < -1 \\ 1+f_c\tau & \text{if } -1 \le f_c\tau < 0 \\ 1-f_c\tau & 0 \le f_c\tau < 1 \\ 0 & 1 \le f_c\tau \end{cases} \tag{22}$$

Typical code phase offsets used are $\Delta\eta = 0.25/f_c$ (quarter-chip) or $\Delta\eta = 0.5/f_c$ (half-chip).

Typical carrier phase discriminators for use in a PLL are the arctangent discriminator:

$$\Delta\hat{\phi}_d = \text{atan}[Q_k(0)/I_k(0)] \tag{23}$$

and the two-argument arctangent discriminator:

$$\Delta\hat{\phi}_d = \text{atan2}[Q_k(0), I_k(0)] \tag{24}$$

The latter discriminator requires compensation for navigation data bit sign changes.

If there are no multipath effects, then the DLL discriminator in Eq. (21) and the two PLL discriminators in Eqs. (23) and (24) will be reasonably accurate. In the presence of multipath, however, they can lead to systematic errors. These will effectively be biases over the time scale in which the multipath parameters α_m, $\Delta\phi_{\alpha m}$ and $\delta\tau_{\alpha m}$ are constants. These biases can be substantial [3], especially if the RF front-end bandwidth is narrow, on the order of 2 MHz [5]. The goal of the present analysis is to develop alternate discriminators that reduce or even eliminate these biases.

B. Optimal Batch Estimation for DLL/PLL Discriminator with Multipath Mitigation

The new multipath discriminator uses the accumulations measurement model in Eqs. (19a) and (19b) to post the following weighted nonlinear least-squares batch estimation problem:

$$\text{find:} \quad \boldsymbol{x} \tag{25a}$$

$$\begin{aligned} \text{to minimize:} \quad J(\boldsymbol{x}) = \tfrac{1}{2}\sum_{k=1}^{K}\Big(&\{\boldsymbol{z}_{Ik}-\boldsymbol{h}_I[\boldsymbol{x};\bar{\tau}_k,\boldsymbol{r}_a(\bar{\tau}_k)]\}^{\mathrm{T}} \times \\ &R_k^{-1}\{\boldsymbol{z}_{Ik}-\boldsymbol{h}_I[\boldsymbol{x};\bar{\tau}_k,\boldsymbol{r}_a(\bar{\tau}_k)]\} \\ &+\{\boldsymbol{z}_{Qk}-\boldsymbol{h}_Q[\boldsymbol{x};\bar{\tau}_k,\boldsymbol{r}_a(\bar{\tau}_k)]\}^{\mathrm{T}} \times \\ &R_k^{-1}\{\boldsymbol{z}_{Qk}-\boldsymbol{h}_Q[\boldsymbol{x};\bar{\tau}_k,\boldsymbol{r}_a(\bar{\tau}_k)]\}\Big) \end{aligned} \tag{25b}$$

$$\text{subject to:} \quad 0 \le \delta\tau_{\alpha m} \quad \text{for } m = 1, ..., M \tag{25c}$$

$$1 = \hat{\boldsymbol{r}}_0^T\hat{\boldsymbol{r}}_0 \tag{25d}$$

$$1 = \hat{\boldsymbol{r}}_{\alpha m}^T\hat{\boldsymbol{r}}_{\alpha m} \quad \text{for } m = 1, ..., M \tag{25e}$$

The inequality constraints in Eq. (25c) ensure that the multipath signals arrive after the direct signal. The equality constraints in Eqs. (25d) and (25e) ensure that the estimated unit direction vectors obey their normalization constraints. The cost function in Eq. (25b) is the negative natural logarithm of the joint probability density function of the accumulation measurement vectors $\boldsymbol{z}_{I1}$, $\boldsymbol{z}_{Q1}$, $\boldsymbol{z}_{I2}$, $\boldsymbol{z}_{Q2}$, $\boldsymbol{z}_{I3}$, $\boldsymbol{z}_{Q3}$, ..., $\boldsymbol{z}_{IK}$, $\boldsymbol{z}_{QK}$ conditioned on the values in the $\boldsymbol{x}$ vector. Therefore, solution of this problem amounts to maximum likelihood estimation.

The minimization of $J(\boldsymbol{x})$ with respect to $\boldsymbol{x}$ is accomplished using a general nonlinear numerical optimization procedure. It is a Newton-based procedure that starts with a guess of the truncated solution vector

$$\boldsymbol{x}_{sht} = \begin{bmatrix} \Delta\omega_{nom} \\ \Delta\gamma_{nom} \\ \Delta\tau_d \\ \hat{\boldsymbol{r}}_0 \\ \Delta\omega_{\alpha 1} \\ \delta\tau_{\alpha 1} \\ \hat{\boldsymbol{r}}_{\alpha 1} \\ \vdots \\ \Delta\omega_{\alpha M} \\ \delta\tau_{\alpha M} \\ \hat{\boldsymbol{r}}_{\alpha M} \end{bmatrix} \tag{26}$$

This vector has dimension (6+5M). It is formed by deleting the phasor components X_d, Y_d, $X_{\alpha 1}$, $Y_{\alpha 1}$, ..., $X_{\alpha M}$, and $Y_{\alpha M}$ from $\boldsymbol{x}$. For any given guess of the optimal value of $\boldsymbol{x}_{sht}$, the exact optimal estimates of these phasor components can be computed analytically by using linear algebra because the phasor components all enter the measurement models in Eqs. (19a) and (19b) linearly. The linear least-squares matrix calculations that are needed to compute these values are described in Ref. 8.

The nonlinear optimization procedure starts with a guess of $\boldsymbol{x}_{sht}$. For each guess, it computes the optimal phasor components. Next, it computes first and second derivatives of the cost function with respect to $\boldsymbol{x}_{sht}$ under the assumption that any variations of $\boldsymbol{x}_{sht}$ will be accompanied by variations of the phasor components in order to maintain their optimality. These partial derivatives can be computed from the partial derivatives with respect to the full $\boldsymbol{x}$ vector. The optimization procedure uses the resulting quadratic approximation to compute updates to its current $\boldsymbol{x}_{sht}$ guess, and iterates until it reaches a local minimum [8,9].

The quadratic approximation of the cost function valid in the vicinity of the current guess of $\boldsymbol{x}_{sht}$ employs the Hessian of the Lagrangian function that is created by adjoining the constraints in Eqs. (25d) and (25e) to the cost. The Hessian matrix has the beneficial effect of approximating the cost impact of brute-force re-normalization of the improved guesses of the $\hat{\boldsymbol{r}}_0$ and $\hat{\boldsymbol{r}}_{\alpha m}$ vectors at the new improved solution guess. The quadratic program that is solved to compute a new solution guess also includes first-order, linearized approximations of the constraints in Eqs. (25d) and (25e). Therefore, the brute-force re-normalization amounts to only a second-order correction.

The particular version of Newton's method that has been used is a trust-region method [8,9,10]. This method explicitly restricts the magnitude of each increment to $\boldsymbol{x}_{sht}$ during the calculation of that increment. The restriction seeks to stay within the region of validity of the local quadratic cost function approximation. The restriction ensures global convergence of the algorithm to at least a local minimum of $J(\boldsymbol{x})$.

C. Generation of Nonlinear Optimal Solution Initial Guesses for Successively Larger Numbers of Multipath Components

A reasonable strategy for estimating the direct and multipath components is to start with the assumption of no multipath, estimate the direct-signal parameters, and then successively add additional multipath components to the problem, estimating each new component's parameters while refining the estimates of the parameters of the previously modeled components. This is similar to the strategy mentioned in Ref. 3 of estimating one multipath component at a time and then subtracting its effects from the accumulations prior to estimating the next component. In that approach, the process of estimating the new component's parameters does not affect the estimates already obtained for other components, which is sub-optimal.

There are also benefits in terms of general nonlinear optimal estimation to the strategy of increasing the number of multipath components in increments of $\Delta M = 1$. One of the main challenges in nonlinear estimation is to start the nonlinear estimation algorithm with a sufficiently good first guess to achieve convergence to the globally minimizing solution of the cost function. In practice, this can be hard to achieve, e.g., see Ref. 10. In the present case, one can use the following initial guess for the truncated solution vector of Eq. (26) when there are no multipath components:

$$(\boldsymbol{x}_{sht})_{guess0} = \begin{bmatrix} (\Delta\omega_{nom})_{guess} \\ (\Delta\gamma_{nom})_{guess} \\ (\Delta\tau_d)_{guess} \\ (\hat{\boldsymbol{r}}_0)_{guess} \end{bmatrix} = \begin{bmatrix} 0 \\ 0 \\ 0 \\ A_{body/ref}(\hat{\boldsymbol{r}}_0)_{ref} \end{bmatrix} \tag{27}$$

where $(\hat{\boldsymbol{r}}_0)_{ref}$ is the known unit direction vector from the satellite to the receiver in some reference coordinate system, perhaps WGS-84 coordinates or local-level coordinates, and where $A_{body/ref}$ is an estimate of the 3-by-3 direction cosines matrix for transformation from the reference coordinate system to the body coordinate system in which the antenna motion time history $\boldsymbol{r}_a(t)$ is defined. Often one has a rough idea of the correct matrix. It can have errors as large as 10 degrees per axis and still provide an adequate first guess for nonlinear algorithm convergence. In the cases considered in Section V, the accuracy appears to have been about 16 deg of total 3-axis rotation error in one case and 8 degrees in the second case.

The first guesses of the other three parameters in Eq. (27), $\Delta\omega_{nom}$, $\Delta\gamma_{nom}$, and $\Delta\tau_d$, are all zero. These constitute good guesses under the reasonable assumption that the PLL and the DLL tracking errors are small enough to maintain lock.

Starting from the first guess in Eq. (27), the optimization problem Eqs. (25a)-(25e) can be solved for the $M = 0$ multipath components case. Next, suppose that the optimal solution for the case of M multipath components is designated as $(\boldsymbol{x}_{sht})_{optM}$. Then one can generate candidate solutions for the case of M+1 multipath components as:

$$(\boldsymbol{x}_{sht})_{guessM+1} = \begin{bmatrix} (\boldsymbol{x}_{sht})_{optM} \\ (\Delta\omega_{\alpha M+1})_{guess} \\ (\delta\tau_{\alpha M+1})_{guess} \\ (\hat{\boldsymbol{r}}_{\alpha M+1})_{guess} \end{bmatrix} \tag{28}$$

The two scalar guess components $(\Delta\omega_{\alpha m+1})_{guess}$ and $(\delta\tau_{\alpha m+1})_{guess}$ and the 3-by-1 unit direction vector guess $(\hat{\boldsymbol{r}}_{\alpha M+1})_{guess}$ can be generated randomly. Uniform distributions can be used to sample guesses of $(\Delta\omega_{\alpha m+1})_{guess}$ and $(\delta\tau_{\alpha m+1})_{guess}$. Reasonable limits for the uniform $(\Delta\omega_{\alpha m+1})_{guess}$ distribution might be $-2\pi/(\bar{\tau}_K - \bar{\tau}_1)$ to $+2\pi/(\bar{\tau}_K - \bar{\tau}_1)$, that is, +/- one full cycle of relative carrier phase during the batch estimation interval, which assumes a length interval on the order of typical multipath-induced amplitude oscillations for a static receiver. Reasonable limits for the uniform $(\delta\tau_{\alpha m+1})_{guess}$ distribution might be $0.01/f_c$ to $0.25/f_c$, that is, from one hundredth of a chip later than the direct signal to one quarter of a chip later. The unit direction vector guess $(\hat{\boldsymbol{r}}_{\alpha M+1})_{guess}$ can be generated by sampling from a zero-mean, identity-covariance 3-by-1 vector Gaussian distribution and then normalizing the result. Such a sampling procedure produces a uniform distribution of directions on the unit sphere.

One could simply re-start the nonlinear solver of the optimization problem in Eqs. (25a)-(25e) using a randomized first guess of the new multipath components, as in Eq. (28). A better approach, however, is to generate multiple randomized first guesses as in Eq. (28) and to perform a quick check of the goodness of each guess by solving a greatly simplified optimization problem. A suitable problem is that of optimizing the weighted fit-error in Eqs. (19a) and (19b) only with respect to the phasors of the new multipath component, $X_{\alpha M+1}$ and $Y_{\alpha M+1}$. This optimization can be carried out in closed form very quickly because these phasors enter the measurement model in Eqs. (19a) and (19b) linearly. The resulting partially optimized costs can be catalogued for many randomized first guesses of the form in Eq. (28). The guess that gives the lowest partially optimized cost is then used as the first guess for a full nonlinear solution of the optimization problem in Eqs. (25a)-(25e).

The combined optimization procedure with generation of successive first guesses for problems with successively larger numbers of multipath components is as follows:

1. Set $M = 0$ and generate the first guess $(\boldsymbol{x}_{sht})_{guess0}$ using. Eq. (27).
2. Solve the M-multipath-component nonlinear optimal estimation problem in Eqs. (25a)-(25e) by using the trust-region method starting from the guess $(\boldsymbol{x}_{sht})_{guessM}$. Designate the resulting solution as $(\boldsymbol{x}_{sht})_{optM}$.
3. Decide whether enough multipath components have been included. If so, then terminate with the solution $(\boldsymbol{x}_{sht})_{optM}$. Otherwise, proceed to Step 4.
4. Generate N randomized first guesses of the M+1-multipath-component problem as defined in Eq. (28) and in the text that follows that equation. Designate them as $[(\boldsymbol{x}_{sht})_{guessM+1}]_n$ for $n = 1, ..., N$.
5. For each $n = 1, ..., N$, substitute $[(\boldsymbol{x}_{sht})_{guessM+1}]_n$ into Eqs. (19a) and (19b) for $k = 1, ..., K$ along with the optimal phasor estimates that are associated with $(\boldsymbol{x}_{sht})_{optM}$, X_{dopt}, Y_{dopt}, $X_{\alpha 1opt}$, $Y_{\alpha 1opt}$, ..., $X_{\alpha Mopt}$. Minimize the weighted sum-squared-error cost function for the resulting equations, as per Eq. (25b) in order to determine the rough estimates $[X_{\alpha M+1roughopt}, Y_{\alpha M+1roughopt}]_n$ and the associated costs $(J_{rough})_n$ for $n = 1, ..., N$.
6. Choose $(\boldsymbol{x}_{sht})_{guessM+1} = [(\boldsymbol{x}_{sht})_{guessM+1}]_{nopt}$, where n_{opt} is chosen so that $(J_{rough})_{nopt} \leq (J_{rough})_n$ for $n = 1, ..., N$.
7. Increment M and go to Step 2.

D. Cost Function Second Derivative, Estimation Error Covariance, and Observability

An advantage of using maximum-likelihood estimation to compute the estimate of $\boldsymbol{x}$ is that the procedure also yields an approximation of the error covariance in these estimates:

$$P_{xx} = E\{(\hat{\boldsymbol{x}}-\boldsymbol{x})(\hat{\boldsymbol{x}}-\boldsymbol{x})^{\mathrm{T}}\} \cong Q\left[Q^{\mathrm{T}}\frac{\partial^2 J}{\partial \boldsymbol{x}}Q\right]_{\hat{\boldsymbol{x}}}^{-1}Q^{\mathrm{T}} \qquad (29)$$

where $\hat{\boldsymbol{x}}$ is the estimate of the true $\boldsymbol{x}$ that solves the optimal estimation problem in Eqs. (25a)-(25e), but with the vector of unknowns expanded to include the phasors, as in Eq. (20). The formula in Eq. (29) is, in effect, an approximation of the Cramer-Rao lower bound for the estimation error covariance [11]. The matrix Q in Eq. (29) is an orthonormal matrix of dimension (8+6M)-by-(7+5M). It is constructed so that its columns are all of unit magnitude, all perpendicular to each other, and all perpendicular to the linearized versions of the unit-normalization constraints in Eqs. (25d) and (25e) as evaluated at the optimal estimate $\hat{\boldsymbol{x}}$. The covariance calculation in Eq. (29) uses Q in order to properly account for the fact that there is no uncertainty about $\hat{\boldsymbol{x}}$ along the M+1 sub-space directions that correspond to the lengths of the vectors $\hat{\boldsymbol{r}}_0$ and $\hat{\boldsymbol{r}}_{\alpha m}$ for $m = 1, ..., M$.

The observability of the batch estimation vector in Eq. (20) can be evaluated using Eq. (29). Observability is the condition of having the vector x uniquely determinable from a set of accumulation vectors $\boldsymbol{z}_{Ik}$ and $\boldsymbol{z}_{Qk}$ for $k = 1, ..., M$, as per the model in Eqs. (19a) and (19b). This uniqueness is equivalent to having a well-defined unique minimum to the cost function $J(\boldsymbol{x})$ in Eq. (25b). Locally, uniqueness is assured if the projected Hessian matrix of the cost function is positive definite, with projection being the operation of limiting the possible x variations to the local tangent space of the unit-normalization constraints in Eqs. (25d) and (25d). The requisite projected Hessian is

$$H_{proj} = Q^{\mathrm{T}}\frac{\partial^2 J}{\partial \boldsymbol{x}}Q \qquad (30)$$

If this matrix is positive definite, then the covariance matrix in Eq. (29) will be positive semi-definite, with its zero eigenvalues along the directions defined by $\hat{\boldsymbol{r}}_0$ and $\hat{\boldsymbol{r}}_{\alpha m}$ for $m = 1, ..., M$. Therefore, the local observability condition and the condition amounts to the condition that the covariance determined in Eq. (29) be positive semi definite.

Many solutions to the nonlinear optimization problem in Eqs. (25a)-(25e) have been calculated, and the positive definiteness of the projected Hessian H_{proj} has been tested at each solution. In all but a few perverse cases that failed to converge to an optimal solution, the positive definiteness of H_{proj} has been confirmed. Therefore, the multipath parameter vector in Eq. (20) is observable based on the measurement model in Eqs. (19a) and (19b) provided that enough samples are included.

Note that it is likely that the observability will vary with the interval of the batch estimation problem and with the richness of the $\boldsymbol{r}_a(t)$ antenna motion. Studies of these relationships are beyond the scope of the present paper.

IV. DATA COLLECTION AND PRE-PROCESSING FOR MULTIPATH ESTIMATION

A. Hardware, Locations, and Experiments

Data for multipath estimation was collected on Sept. 6, 2013 on the Cornell University campus at two distinct locations. The first set of data was collected in front of Cornell's Rhodes Hall as seen in Fig. 5. The second set of data was collected on the roof of Rhodes Hall as seen in Fig. 6. The first location was expected to have a more significant multipath interference environment due to the presence of a tall building nearby.

Fig. 5. Data collection system, seen in front of Rhodes Hall in Ithaca, NY.

A patch antenna mounted on a ground-plane plate was used to receive the GPS signals. As seen in Fig. 5 and Fig. 6, this mounting plate was bolted to the top of the motion system -- the ground plane plate is visible in both figures, but the patch antenna is not visible because it is shielded from the camera's view by the plate below it.

The motion system consisted of 3 independent stepper motors connected to 3 threaded rods individually. The local body-fixed coordinates system of the motion device, the one in which $\boldsymbol{r}_a(t)$ is defined, has its x axis aligned with the horizontal threaded rod that is parallel to the road in Fig. 5, and +x pointing towards the bottom left of Fig. 5, which is roughly north. The +z axis points upwards along the vertical beam of the system. The y axis lies along the horizontal threaded rod that is perpendicular to road in Fig. 5, and its positive direction is towards the right of the figure, making the coordinate system right-handed.

Fig. 6 Data collection system, seen on the roof of Rhodes Hall in Ithaca, NY.

One run of the motion system consists of moving successively 10 cm in +x, +y, -z, -x, -y and +z axes in the local body-fixed coordinate system. This set of movements lasted approximately 25 seconds.

For each of the two experiment locations, the motion system was run 3 times, with pauses of no movement in between, while data were collected. This set of 3 movements with pauses in between lasted approximately 5 minutes for each location.

B. Data and Data Processing

Wide-band RF data were recorded on disk and saved for post-processing. The timing of the data capture was synchronized to the timing of the antenna motion to within about 1 second.

Collected GPS RF data were processed offline using a C-language GPS software radio receiver in order to produce pseudorange, negative beat carrier-phase, and I and Q accumulations at a 100 Hz cadence for all available signals. Five signals were available from the ground-level tests in front of Rhodes Hall, and nine signals were available from the rooftop tests.

Thirty one code delay offsets from the DLL prompt code were used to compute accumulations, $\eta = -1/f_c$, $\eta = -(14/15)/f_c$, $\eta = -(13/15)/f_c$, ..., $\eta = +1/f_c$. That is, offsets were calculated spanning from 1 chip early relative to prompt all the way to 1 chip late. The intervals between code offsets were 1/15th of a chip.

Two pre-processing calculations were implemented in order to save nonlinear optimization computation time. Both of them reduce the number of accumulation measurements in the batch cost function in Eq. (25b). One calculation reduces the [I;Q] sampling rate from 100 Hz to 20 Hz via accumulation over successive sets of five 100 Hz accumulations to produce 20 Hz accumulations. This operation has the effect of reducing the total sample count K in the batch optimization problem by a factor of 5. The additional coherent integration is carried out after navigation data bit wipe-off. It does not cause a significant loss of optimal estimation accuracy due to the low bandwidth of the $\boldsymbol{r}_a(t)$ motion history, which is much lower than 20 Hz.

Another computation time savings reduces the number of code delay offsets from L = 31 in the original data set to L = 11. That is, approximately 2/3 of the code offsets are discarded. The final set consists of 11 offsets that span from 1 chip early to 1 chip late relative to prompt with a spacing of 1/5th of a chip between neighboring offsets. This decimation of the code delay offsets is not expected to seriously degrade the estimation accuracy if there are not too many multipath signals because the random noise in the discarded offsets is highly correlated with noise in the remaining samples, as per Eq. (18). If, however, there were many multipath components whose primary differences were their code delays, then this decimation of code delay offsets could have a significant negative impact on the final estimation accuracy.

Additional pre-processing on the [I,Q] accumulations was carried out in order to remove two effects that are not contained in the measurement model in Eqs. (19a) and (19b). One is the fact that the software receiver's PLL had a high enough bandwidth to directly track the beat carrier-phase changes caused by the $\boldsymbol{r}_a(t)$ antenna motion. Thus, the $\boldsymbol{r}_a(t)$ effects all show up in the beat carrier phase observable rather than in the [I,Q] accumulations.

As discussed in Section II, this problem can be remedied by computing the difference between the PLL beat carrier phase and a polynomial fit that matches only the beat carrier phase immediately before and immediately after the $\boldsymbol{r}_a(t)$ motion profile and that smoothly transitions between the before and after phase profiles during the motion sequence. This difference is then used to rotate the [I,Q] accumulation time history in order to re-insert the $\boldsymbol{r}_a(t)$ effects.

This phase difference is shown as the dash-dotted red curve in Fig. 7 for one of the experiments and one of the signals. Also shown in the figure are the detrended PLL carrier phase that includes the $\boldsymbol{r}_a(t)$ effects (solid blue curve) and the curve that fits this latter curve only before and after the $\boldsymbol{r}_a(t)$ motion profile (dashed olive green curve). This latter curve is a fifth-order polynomial fit in the case considered in Fig. 7. The $\boldsymbol{r}_a(t)$ effects are apparent in the solid blue curve from t = 153 sec to t = 178 sec as the large negative excursion from the dashed green curve. The dashed red difference between these two curves is zero before and after the $\boldsymbol{r}_a(t)$ motion, but it includes the $\boldsymbol{r}_a(t)$ dip between t = 153 and 178 sec. This dip in the dash-dotted red curve is used to rotate the PLL-generated [I;Q] accumulations in a way that transfers the $\boldsymbol{r}_a(t)$ effects from the phase observable back into the [I;Q] accumulations.

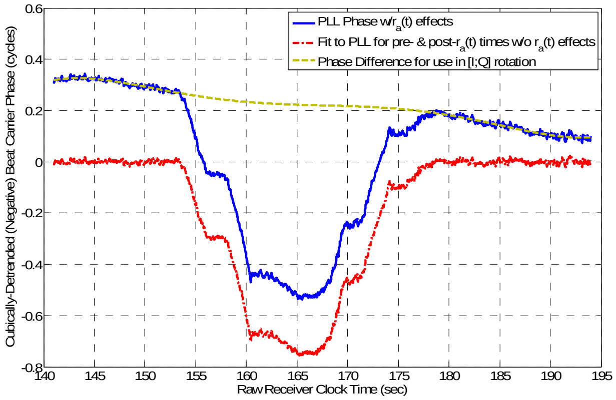

Fig. 7 Detrended (negative) beat carrier phase with (solid blue) and without (dashed-olive) $\boldsymbol{r}_a(t)$ *effects along with phase difference (dash-dotted red) that is used for [I;Q] rotation.*

Also as discussed in Section II, a related correction must be made to the code phases. The multipath effects cause large swings in the DLL's code phase measurements, and these swings violate the Eqs. (19a) & (19b) assumption of a constant offset between the prompt DLL code replica and the true received PRN code. This problem is illustrated by considering the difference between changes in pseudorange and beat carrier phase during the $\boldsymbol{r}_a(t)$ motion profile as shown in Fig. 8. As can be seen from the blue curve in the figure, the pseudorange excursions are large, up to 20 m. Obviously, these are not the direct results of the 10-cm-per-axis $\boldsymbol{r}_a(t)$ motion of the antenna.

A simple technique has been used to approximately repair the modeling discrepancy between Eqs. (19a) and (19b) and the DLL pseudorange excursions shown Fig. 8. It uses the difference between pseudorange and beat carrier phase, as plotted in Fig. 8, to estimate where the DLL would have placed the prompt PRN code had it used carrier aiding exclusively during the $\boldsymbol{r}_a(t)$ motions. It then computes the effective η code phase offsets of the $I_k(\eta)$ and $Q_k(\eta)$ accumulations computed in Eqs. (2a) and (2b). These effective values are then used to interpolate the accumulations back onto the original set of η grid points in order to approximate the accumulations that would have been computed in Eqs. (2a) and (2b) had the DLL positioned its prompt PRN code using carrier aiding exclusively. Once this has been done, the accumulations models in Eqs. (19a) and (19b) are fairly well satisfied. Note, however, that this procedure leaves the direct $\boldsymbol{r}_a(t)$ effects in the effective DLL determination of the prompt code phase, which technically violates an assumption of Eqs. (19a) and (19b). Fortunately, given the 10 cm motion level of $\boldsymbol{r}_a(t)$, this modeling discrepancy will have only a negligible impact in the multipath estimation results for C/A code that are presented in Section V.

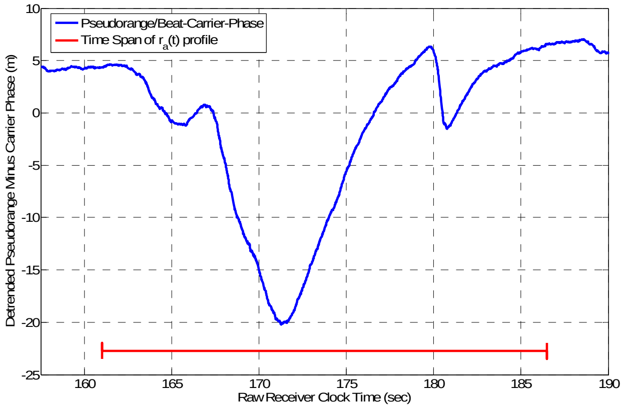

Fig. 8 Excursions of DLL pseudorange during an $\boldsymbol{r}_a(t)$ motion profile as measured relative to beat carrier phase.

C. Antenna Location Determination

Unfortunately, the motion system did not include a position feedback sensor. There was a known pre-specified motion profile, but there was a question about how accurately the device followed the planned profile. There was also an unknown timing bias between the motion profile and the GPS data capture device of about 1 second. In addition, the tall beam on which the antenna stood was prone to oscillations along its most flexible axis, i.e., along the horizontal y axis. These oscillations tended to occur at the start and stop of the y-axis motion intervals, and their magnitude and frequency were unmeasured and unmodeled.

Given the importance of knowing $\boldsymbol{r}_a(t)$ and given the lack of precision with which this profile could be known a priori and the lack of a direct $\boldsymbol{r}_a(t)$ measuring system, Carrier-phase Differential GPS (CDGPS) techniques were used to estimate the $\boldsymbol{r}_a(t)$ profile. A special RTK-like CDGPS algorithm was developed and applied to the roof-top data, where data from 9 satellites were available. This special algorithm did not use receiver-to-receiver differencing. Instead, it used satellite-to-satellite differencing, a polynomial fit to residual non-motion-induced carrier-phase variations, and the information that certain data points at the start and stop of a given motion interval corresponded to the same at-rest machine position. The CDGPS algorithm solved for the motion profile relative to this at-rest position. This definition of the relative motion, when coupled to the fact that the device started at its rest position and returned to it at the end of its motion profile, amounted to a sort of second differencing in time of the beat carrier phases in the CDGPS solution algorithm.

The result of the CDGPS calculation was a fairly consistent set of profiles for the 3 roof-top cases. These profiles were averaged in order to determine a presumed machine motion profile. The original profiles were estimated in local vertical-east-north coordinates. Next, they were averaged using an algorithm that also found their optimal relative timing alignments. Finally, an orthonormal coordinate transformation from vertical-east-north coordinates to machine coordinates was estimated by exploiting the presumption that the main features of the motion profile in machine coordinates were successive ramps along +x, +y, -z, -x, -y, and +z. This coordinate transformation was used to transform the averaged motion profile into machine coordinates. The resulting profile appears in Fig. 9 along with the 3 per-case profiles that were average in order to determine the final profile.

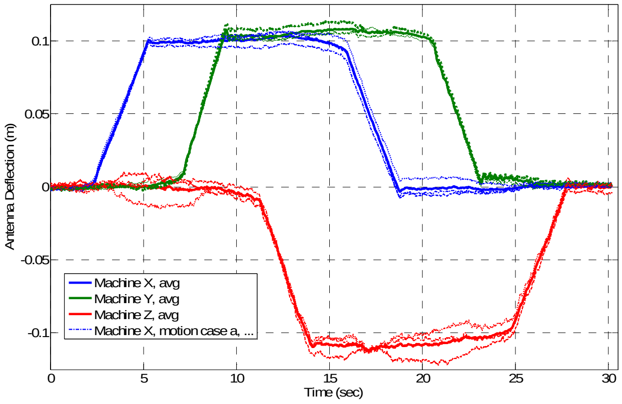

Fig. 9 Receiver antenna motion profile as determined from CDGPS calculations applied to 3 roof-top motion cases followed by averaging and coordinate transformation.

It is apparent from Fig. 9 that the pre-programmed sequence of 10 cm motion along the successive axis +x, +y, -z, -x, -y, and +z is consistent with the CDGPS results. Also, the differences between the individual cases and the averaged result is no greater than 1.5 cm, and usually it is much smaller. Also, small oscillations in the green y-axis curves are apparent after the end of its initial ramp at t = 9 sec and especially after the end if its final ramp at t = 23 sec. Therefore, these solved-for motion profiles seem reasonable for use in the multipath estimation algorithm.

Of course, there is an open question about the effects of multipath on this CDGPS-based estimate of the $\boldsymbol{r}_a(t)$ motion profile. Given that $\boldsymbol{r}_a(t)$ needs to be known in order to estimate multipath, it seems questionable to use a method of determining $\boldsymbol{r}_a(t)$ that is susceptible to multipath errors. In truth, it would be best to have an independent, non-GPS method of determining $\boldsymbol{r}_a(t)$ accurately. The only reason for resorting to CDGPS to determine $\boldsymbol{r}_a(t)$ was due to the lack of an $\boldsymbol{r}_a(t)$ sensor. In the future, it will be utmost importance to do additional experiments with such a sensor.

In the mean time, it is hoped that the errors in this CDGPS solution for $\boldsymbol{r}_a(t)$are small due to several factors: the likelihood of lower multipath on the Rhodes Hall rooftop, the use of 9 satellite signals to compute the CDGPS solution, and the averaging of 3 different runs carried out over a 5 minute interval, a long enough interval for multipath errors to change from run to run. The averaged CDGPS profile does match the pre-programmed profile fairly closely even though the CDSGPS calculations had no information about the profile other than the fact that it started and stopped in the same location. Therefore, one might surmise that the multipath effects were not great enough to cause serious problems with this technique of determining $\boldsymbol{r}_a(t)$. Further evidence supporting this conjecture is found in the attempt to match profiles for the 3 cases that were run in the high-multipath environment in front of Rhodes Hall. The matching was much poorer than in Fig. 7.

V. EXPERIMENTAL MULTIPATH ESTIMATION RESULTS

The nonlinear optimal estimation algorithm of Section III has been applied to the experimental data described in Section IV, and the results have been analyzed to assess the effectiveness of the multipath estimation algorithms. Assessment of experimental results, however, is a challenge. There is no known "truth" value for the multipath components. Even the direct-path signal's truth parameters are uncertain due to the uncertainty of things such as the unknown attitude of the machine coordinate system measured relative to reference coordinates. Therefore, it is a challenge to find and apply effective method of assessing performance.

Four methods have been used to assess performance. The first is residuals assessment. It considers the optimal fit errors at the final value of the optimal cost in Eq. (25b) and whether they are statistically reasonable. The second assessment method considers the reasonableness of the computed estimation parameters, that is, of the individual elements of the $\boldsymbol{x}_{opt}$ vector. The third assessment metric considers the estimated directions of arrival of the direct signals, the $\hat{r}_{0opt}$ elements of $\boldsymbol{x}_{opt}$. Their reasonableness can be checked by comparing the angles between estimates for multiple signals with the corresponding known angles in reference coordinates. The fourth method of assessment is to compute the wideband pseudorange from the $[I;Q]$ accumulation after subtraction of the optimally estimated multipath components. The resulting corrected accumulations can be used in a DLL-discriminator-type calculation. A good multipath solution should reduce the influence of multipath on the resulting pseudorange estimates.

Other methods of evaluation might have been applied had the experimental set-up been different. One would be to operate the moving-antenna system near a known strong reflector, such as a calm body of water or a building with a large flat metallic surface. The estimated relative delay and direction of arrival of the multipath signal could then be compared with the expected values based on the geometry of the reflective surface relative to the satellite direction and the receive location. Alternatively, one could operate the system on two successive days at the exact same location and exactly 24 sidereal hours apart. The GPS satellites' repeated ground tracks typically cause the multipath to repeat. The system's estimated multipath parameters could be compared over the two successive days' runs to see if the multipath parameters repeat. Unfortunately, the experimental data collection campaign reported here was not structured to exploit either of these possibilities.

A. Optimized Cost Function Residuals

Statistical analysis predicts that the optimized value of the optimal cost in Eq. (25b), if doubled, should be approximately a sample from a chi-squared distribution with degree $2KL - 7M - 8$. This is true because the residual fit error should be caused primarily by Gaussian random noise, because $(R_k)^{-1}$ matrix in Eq. (25b) normalizes the residual Gaussian noise to have an identity covariance matrix, and because there are independent $2KL$ accumulation measurements in the entire data batch and $7M$+8 estimated quantities in the estimation problem. Therefore, the expected mean value of the optimal cost is $0.5(2KL-7M-8)$. If the measurement model in Eqs. (19a) and (19b) captures most of what is happening, then the actual value of $J(\boldsymbol{x}_{opt})$ computed using data will be near the expected value. Therefore, assessment of the residuals provides a check on the multipath model's reasonableness for an actual experiment.

Visually, one can assess fit errors between measured and modeled by considering plots of I and Q accumulations. Consider Fig. 10 and Fig. 11. They plot the prompt accumulation amplitude time histories, $[I_k^2(0)+Q_k^2(0)]^{1/2}$ vs. $\bar{\tau}_k$, for two cases. Fig. 10 is for PRN 32 when operating the moving-antenna system in front of Rhodes Hall, which is considered to be a high multipath environment. Fig. 11 applies to PRN 28 when the system is operating on the roof of Rhodes Hall, a lower multipath environment. Each of the figures plots 6 amplitude time histories. The red dots are the actual prompt accumulation amplitude data. The solid turquoise curve is the optimal amplitude estimate under the assumption of no multipath. The other 4 curves correspond to 4 different numbers of estimated multipath components, M = 1 (dashed green curves), M = 2 (dash-dotted blue curves), M = 3 (dotted black curves) and M = 4 (dashed magenta curves).

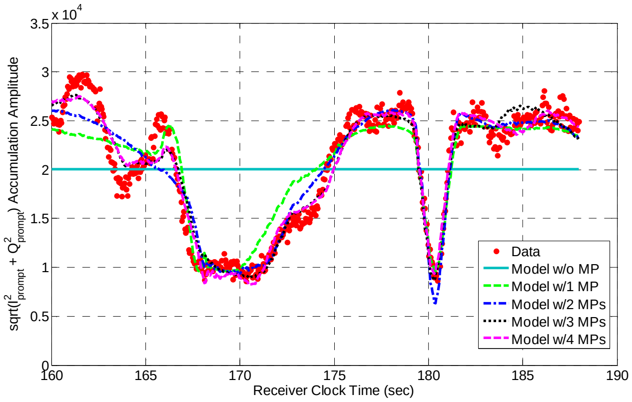

Fig. 10 Measured and optimal-fit prompt accumulation amplitude times histories for PRN 32 in front of Rhodes Hall.

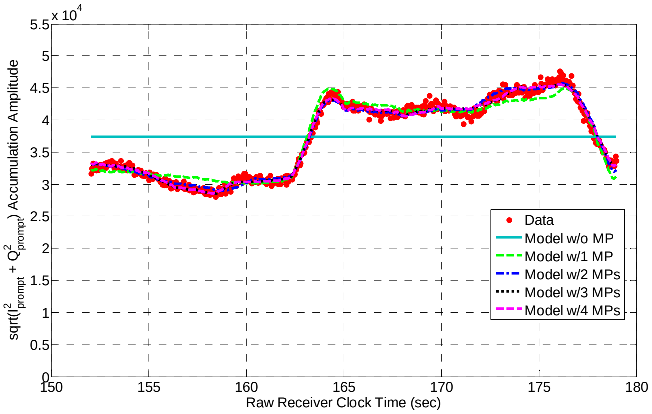

Fig. 11. Measured and optimal-fit prompt accumulation amplitude times histories for PRN 28 on roof of Rhodes Hall.

In both of these cases, the models that assume multipath fit the prompt accumulation data better than the model that assumes only a direct component. The actual data have a time-varying amplitude in both cases, likely due to multipath error, but the model with no multipath cannot account for such variations. Therefore, its value is just a constant that tries to fit the mean value of the fluctuating amplitude. The successive multipath estimates fit the amplitude better as the assumed number of multipath components M increases. In the high multipath environment of Fig. 10, the fit error makes noticeable improvements as M is increased from 1 to 4. Note how the dashed magenta curve fits the data very well after t = 166 sec. Only the dashed magenta curve and the dotted black curve have remotely reasonable fits to the first to amplitude oscillations before t = 166 sec, and the dashed magenta curve fits the data best after t = 182 sec. In Fig. 11, the fit errors are small for all $M \geq 2$. Note how the dash-dotted blue curve, the dotted black curve, and the dashed magenta curve all fit the red dots well for the entire data batch. In both of these cases, the visual fits indicate that the multipath model successfully accounts for the observed data provided it includes enough multipath components.

The optimal residuals ratio $\gamma_M = J(\boldsymbol{x}_{opt})/(KL\text{-}3.5M\text{-}4)$ tells a similar story. For Fig. 10, the respective values of γ_0 to γ_4 are 10.27, 3.96, 2.53, 1.88, and 1.68. This clearly indicates an increasing goodness of fit as M increases. Unfortunately, chi-squared probability theory indicates that γ_4 should be below 1.0399 in 999 out of 1000 samples. Therefore, the fit error ratio 1.68 is still unreasonably large. This is illustrated visually in Fig. 10 by the fact that the excursions of the dashed magenta curve from the red dots is sometime significantly larger than the random statistically spread of the data points. The multipath model with M = 4 multipath components does not full account for the data collected in this case. Fig. 11 appears to be better in this respect, but its corresponding γ_0 to γ_4 values are 15.00, 2.73, 2.24, 2.14, and 2.11. Again, fit error improves with increasing M, but it is not nearly as good as it should be based on statistical analysis; γ_4 should be less than 1.0406 in 99.9% of cases.

Accumulation data have been optimally processed and residuals have been considered for every tracked satellite for the middle motion profiles in each experiment location, in front of Rhodes Hall and the Rhodes Hall roof. The 5 satellites tracked in front of Rhodes Hall were PRNs 17, 20, 24, 28, and 32. All of them experience improved fits/decreased residuals with increases of M up to 4, but none of them produced a γ_4 value that was statistically reasonable. The lowest achieved value was γ_4 = 1.54 for PRN 24, but in that situation with the 99.9% chi-squared threshold was much smaller, 1.04. Thus, the multipath model in Eqs. (19a) and (19b) does not capture all that is occurring in these situations. Furthermore, the nonlinear optimal estimation algorithm experienced convergence difficulties in a few cases: in the M = 3 and M = 4 cases for PRN 17 and in the M = 4 cases for PRNs 24 and 28. Their convergence was very slow. This issue will be discussed more in the next subsection.

The 9 satellites tracked from the roof of Rhodes Hall were PRNs 01, 02, 04, 10, 12, 17, 20, 24, and 28. Like the data from in front of Rhodes Hall, these all experience reduced fit residuals with increases in the number of multipath components M. Unlike the data from the front of Rhodes, 6 of these 9 satellites reached statistically reasonable γ_M values for $M \leq 4$. PRNs 02, 10, and 17 achieved statistically reasonable data fits for $M = 2$ multipath components, PRNs 20 and 24 achieved reasonable fits for $M = 3$ components, and PRN 04 achieved a reasonable fit at $M = 4$. Thus, the model in Eqs. (19a) and (19b) appears to match the data more closely in the relatively benign multipath environment on the Rhodes Hall roof.

It should also be noted that a few of the accumulation amplitude fits appeared much poorer visually than those shown in Fig. 10 and Fig. 11. In particular, PRN 20's amplitude fits are particular poor for all cases $M = 0$ to 4 for the middle motion profile in front of Rhodes Hall. As yet, there is no explanation for why this occurs.

B. Reasonableness of Estimates in $\boldsymbol{x}_{opt}$

The present section considers the reasonableness of the optimal estimates of the various elements of the x vector that is defined in Eq. (20). For purposes of this analysis, these elements can be considered in groups. The first group is that of Doppler shift and Doppler-shift rate elements. This group consists of $\Delta\omega_{nom}$, $\Delta\gamma_{nom}$, $\Delta\omega_{\alpha 1}$, $\Delta\omega_{\alpha 2}$, ..., $\Delta\omega_{\alpha M}$. The second group consists of the code delays in $\Delta\tau_d$, $\delta\tau_{\alpha 1}$, $\delta\tau_{\alpha 2}$, ..., $\delta\tau_{\alpha M}$. The third group consists of the direction-of-arrival unit vectors in $\hat{\boldsymbol{r}}_0$, $\hat{\boldsymbol{r}}_{\alpha 1}$, $\hat{\boldsymbol{r}}_{\alpha 2}$, ..., $\hat{\boldsymbol{r}}_{\alpha M}$. The fourth group consists of the phasors $[X_d;Y_d]$, $[X_{\alpha 1};Y_{\alpha 1}]$, $[X_{\alpha 2};Y_{\alpha 2}]$, ..., $[X_{\alpha M};Y_{\alpha M}]$.

There are no particular characteristics to expect for the Doppler-shift and Doppler-shift-rate parameters $\Delta\omega_{nom}$, $\Delta\gamma_{nom}$, $\Delta\omega_{\alpha 1}$, $\Delta\omega_{\alpha 2}$, ..., $\Delta\omega_{\alpha M}$ except that they be reasonably small. Small is defined in terms of the aliasing that occurs at half the accumulation frequency, i.e., at $\pi/(\bar{\tau}_{k+1} - \bar{\tau}_k)$. All of the estimated Doppler parameters $\Delta\omega_{nom}$, $\Delta\omega_{\alpha 1}$, $\Delta\omega_{\alpha 2}$, ..., $\Delta\omega_{\alpha M}$ have absolute values less than 1% of this aliasing frequency. In fact, all have absolute values less than $4\pi/(\bar{\tau}_K - \bar{\tau}_1)$ so that none of can produce more than 2 full oscillations over the entire estimation data batch. The estimated $\Delta\gamma_{nom}$ Doppler shift rate values respect a corresponding limit on their absolute values equal $8\pi/(\bar{\tau}_K - \bar{\tau}_1)^2$. Neither will they produce more than 2 full rotations over the data batch. In practice, these estimates normally produce less than one full phase rotation over the batch interval of the direct signal relative to the PLL phase or of the multipath signals relative to the direct signal.

The estimated absolute direct-signal code delays in $\Delta\tau_d$ and the estimated multipath code delays in $\delta\tau_{\alpha 1}$, $\delta\tau_{\alpha 2}$, ..., $\delta\tau_{\alpha M}$ take on reasonable values for all cases considered. The estimates of the multipath-induced DLL code errors represented by $\Delta\tau_d$ are typically on the order of 0.01 chips or less. The multipath code phase delay estimates in $\delta\tau_{\alpha 1}$, $\delta\tau_{\alpha 2}$, ..., $\delta\tau_{\alpha M}$ span the range from 0 chips to 1.25 chips.

Evaluation of the reasonableness of the estimated direct-path direction vectors $\hat{\boldsymbol{r}}_0$ is reserved for analysis in the next subsection. The estimated multipath unit direction vectors $\hat{\boldsymbol{r}}_{\alpha 1}$, $\hat{\boldsymbol{r}}_{\alpha 2}$, ..., $\hat{\boldsymbol{r}}_{\alpha M}$ cannot be evaluated for their reasonableness because there is no way to know their true directions in the unstructured environment that has been used to conduct the experiments. It is interesting to note, however, that many of the estimated directions had negative elevations. Elevation could be deduced easily because it was known that the +z axis of the antenna motion device pointed nearly vertical. Therefore, a positive value of the third component of any given $\hat{\boldsymbol{r}}_{\alpha m}$ vector indicated its arrival from a direction of negative elevation. These negative elevations are reasonable because the ground can cause multipath reflections.

Another important phenomenon noted for some of the $\hat{\boldsymbol{r}}_{\alpha m}$ estimates is that they sometimes occurred in closely spaced pairs. This occurred for PRNs 17. 24, and 28 in the high multipath cases in front of Rhodes Hall. In the Rhodes roof data, this situation occurred only for PRN 28. These occurrences are coupled to an even stranger phenomenon in the multipath phasor estimates, and discussion of this phenomenon is left to the discussion of the reasonableness of the phasor estimates.

The estimates of the direct and multipath phasors $[X_d;Y_d]$ and $[X_{\alpha 1};Y_{\alpha 1}]$, $[X_{\alpha 2};Y_{\alpha 2}]$, ..., $[X_{\alpha M};Y_{\alpha M}]$ give information about the carrier phases and amplitudes of the various received signal components. There are no obviously unreasonable values for their atan2(Y,X) phases, but their $(X^2+Y^2)^{1/2}$ amplitudes can be analyzed for reasonableness.

One would expect the direct signal amplitude $(X_d^2+Y_d^2)^{1/2}$ to be significantly larger than any multipath amplitude $(X_{\alpha m}^2+Y_{\alpha m}^2)^{1/2}$. In the majority of cases this is true. In some cases, however, there exists a multipath component with a larger amplitude. Some of these cases are benign. The relative code delay of the offending multipath component is $\delta\tau_{\alpha m} = 0$. This can occur when a multipath component and the direct signal arrive at virtually the same time. There is no way for the batch optimization problem solver associated with Eqs. (25a)-(25e) to distinguish which signal is the multipath signal and which is the direct signal. A simple comparison of amplitudes, however, can be used to distinguish the direct-path signal when $\delta\tau_{\alpha m} = 0$. The direct-path signal is larger. In every case where this occurred, the conjecture that the signal with the largest amplitude was the direct-path signal was confirmed by comparing its direction of arrival with the expected direction of arrival of the direct-path signal.

This comparison used analyses similar those described in the next subsection.

In most of cases that have been analyzed, including the benign cases of a reversible mis-identification of the true direct signal, the multipath signal amplitudes range from less than 5% of the true direct-path amplitude to as much a 75%. In most cases the multipath components all have amplitudes that are less than 50% of the direct path amplitudes. These appear to be reasonable results.

Another type of larger multipath amplitude also occurs, one that is not benign. In this case, two multipath components have larger amplitudes than the direct path, much larger, perhaps several orders of magnitude larger. These multipath signals can have non-negligible delays $\delta\tau_{\alpha m}$ past the direct-path signal. In every such case, the two large-amplitude multipath signals also have nearly identical directions of arrival $\hat{\boldsymbol{r}}_{\alpha m}$, as already noted for PRNs 17. 24, and 28 in front of Rhodes Hall and for PRN 28 on the roof of Rhodes Hall. They also have nearly opposite carrier phases. That is the $[X_{\alpha m};Y_{\alpha m}]$ phasor of one of these components is almost exactly equal to the negative of the phasor of the other component.

These strange multipath components constitute a sort of multipath doublet. They almost cancel, but they do not quite cancel so that the produce an unusual signal structure that better fits the data. It is conjectured that these are the result of an actual signal phenomenon: diffuse multipath. They may be the estimator's best way to cope with this phenomenon that does not fit into its specular multipath model form.

Regardless of whether or not this phenomenon is diffuse multipath, it presents a significant problem for the estimator. This situation causes very slow progress of the trust-region nonlinear estimation algorithm towards a solution, and it is forced to quit before reaching a true local optimum of the cost function.

This problem of doublets implies that a better understanding of this phenomenon is needed to operate the present algorithms in a high-multipath environment. It is hoped that a better understanding would lead to a capability of adding new terms to the model in Eqs. (19a) and (19b). These new terms would model in a better way the phenomenon that is currently being approximated by multipath doublets. Presumably the new terms would contain unknown parameters that could be estimated in order to perform multipath mitigation.

C. Analysis of Estimated Direct-Signal Arrival Directions

The estimated arrival directions of the direct-path signals are best evaluated simultaneously for all available satellite signals during a given antenna motion profile. Suppose that these estimates are $\hat{\boldsymbol{r}}_{0opt}^{n}$ for $n = 1, ..., N$, where n is the satellite index and where N is the total number of satellites whose signals have been tracked and analyzed to estimate their direct-path and multipath components. Knowledge of the receiver location, the satellite ephemerides, and the time can be used to estimate these same direct-path direction-of-arrival vectors in some known reference coordinate system. Suppose that the chosen reference coordinate system is the local-level vertical/east/north coordinate system, and suppose that the know direction-of-arrival vectors in this system are $\hat{\boldsymbol{r}}_{ven}^{n}$ for $n = 1, ..., N$. The two sets of direction-of-arrival vectors are given in two different coordinate systems, and they can be used to estimation the orthogonal transformation between these systems.

Suppose that $A_{body/ven}$ is the unknown 3x3 orthonormal coordinate transformation matrix from vertical/east/north reference coordinates to the antenna articulation coordinate system in which $\boldsymbol{r}_a(t)$ is defined and in which $\hat{\boldsymbol{r}}_{0opt}^{n}$ for $n = 1, ..., N$ have been estimated by the algorithm of Section III. Then an good estimate of $A_{body/ven}$ can be computed by solving Wahba's problem [12]:

$$\text{find:} \quad A_{body/ven} \tag{31a}$$

$$\text{to minimize:} \quad J(A_{body/ven}) = \tfrac{1}{2}\sum_{n=1}^{N} w_n [\hat{\boldsymbol{r}}_{0opt}^{n} - A_{body/ven}\hat{\boldsymbol{r}}_{ven}^{n}]^{\mathrm{T}} \times [\hat{\boldsymbol{r}}_{0opt}^{n} - A_{body/ven}\hat{\boldsymbol{r}}_{ven}^{n}] \tag{31b}$$

$$\text{subject to:} \quad I = A_{body/ven}^{\mathrm{T}} A_{body/ven} \tag{31c}$$

where the quantities w_n for $n = 1, ..., N$ are positive weights. In the present analysis these weights are set equal to the received carrier-to-noise ratios of the direct-path signals. Thus, stronger signals are deemed to have more accurately determined $\hat{\boldsymbol{r}}_{0opt}^{n}$ vectors. This attitude estimation problem can be solved in closed form using the q-method [13]. The q-method solves for the optimal quaternion representation of $A_{body/ven}$ by solving a related eigenvalue/eigenvector problem for a symmetric 4x4 matrix.

The efficacy of the multipath estimation algorithm of Section III can be evaluated by comparing two solutions to the attitude determination problem in Eqs. (31a)-(31c). One solution uses that $\hat{\boldsymbol{r}}_{0opt}^{n}$ estimates that assume the presence of $M = 0$ multipath signals in the model in Eqs. (19a) and (19b). The other solution uses $\hat{\boldsymbol{r}}_{0opt}^{n}$ estimates that include enough multipath components to achieve a reasonably small optimal cost, and correspondingly, reasonable small measurement error residuals, as discussed in Subsection V.A. The better solution is the one that produces the lowest optimal cost value for the cost function in Eq. (31b). In the limit of small angular errors, this cost is proportional to the mean square of the angular errors between the estimated unit direction vectors $\hat{\boldsymbol{r}}_{0opt}^{n}$ and the corresponding transformed reference coordinates vectors $\hat{\boldsymbol{r}}_{body}^{n} = A_{body/ven}\hat{\boldsymbol{r}}_{ven}^{n}$. A small cost value also indicates that the relative angles between the estimated vectors $\hat{\boldsymbol{r}}_{0opt}^{n}$ for $n = 1, ..., N$ match the relative angles between the original reference vectors $\hat{\boldsymbol{r}}_{ven}^{n}$ for $n = 1, ..., N$. The ability to match these relative angles indicates the reasonableness of the $\hat{\boldsymbol{r}}_{0opt}^{n}$ estimates.

These calculations have been performed for two cases. One case is for the second motion profile on the roof of Rhodes Hall and includes $N = 9$ satellites in the attitude determination problem of Eqs. (31a)-(31c). The choice of multipath solutions for the case that uses $M > 0$ multipath components to form the $\hat{\boldsymbol{r}}_{0opt}^{n}$ estimates was set at $M = 3$ for all satellites except PRN 04. PRN 04 used its $\hat{\boldsymbol{r}}_{0opt}^{n}$ solution from its multipath solution that used was set at $M = 4$ multipath components because 4 components seemed necessary to get a reasonable low residuals fit. This case yielded an RMS angular error between its estimated $\hat{\boldsymbol{r}}_{0opt}^{n}$ vectors and its transformed reference vectors $\hat{\boldsymbol{r}}_{body}^{n}$ of 4.8 deg when using the $\hat{\boldsymbol{r}}_{0opt}^{n}$ that assumed no multipath components in problem (25a)-(25e). When using $\hat{\boldsymbol{r}}_{0opt}^{n}$ that were estimated along with multipath component parameters, however, the RMS angular errors between the $\hat{\boldsymbol{r}}_{0opt}^{n}$ and $\hat{\boldsymbol{r}}_{body}^{n}$ direction vectors was reduced to 2.9 deg. Thus, the multipath estimation problem appears to yield improved direction estimations for its direct-signal components. As a further confirmation of the efficacy of the multipath estimation, the peak angular error between a $\hat{\boldsymbol{r}}_{0opt}^{n}$ vector and its corresponding $\hat{\boldsymbol{r}}_{body}^{n}$ vector was 10.1 deg when multipath was ignored in the estimation of $\hat{\boldsymbol{r}}_{0opt}^{n}$, but it dropped to 5.5 deg when multipath was considered.

The same test was performed for the data from the front of Rhodes Hall. In this case there were only $N = 5$ satellites available. The RMS errors between the $\hat{\boldsymbol{r}}_{0opt}^{n}$ estimates and the transformed reference vectors $\hat{\boldsymbol{r}}_{body}^{n}$ was 8.0 deg for the case that ignored multipath in the estimation of $\hat{\boldsymbol{r}}_{0opt}^{n}$, but it rose to 8.9 deg when multipath components were considered during the estimation of the $\hat{\boldsymbol{r}}_{0opt}^{n}$ vectors. The peak angular errors went the opposite way. The peak was 14.7 degrees for the $\hat{\boldsymbol{r}}_{0opt}^{n}$ vectors that were estimated ignoring multipath, but only 11.3 deg when using the $\hat{\boldsymbol{r}}_{0opt}^{n}$ that were formed while considering multipath effects in the Eqs. (25a)-(25e) optimal estimation problem.

The ability to estimate $\hat{\boldsymbol{r}}_{0opt}^{n}$ accurately by solving the estimation problem in Eqs. (25a)-(25e) serves as a proxy for the ability to remove multipath effects from measured beat carrier phase. In all situations, the ability to resolve $\hat{\boldsymbol{r}}_{0opt}^{n}$ is based primarily on its impact on the carrier phase data that is contained implicitly in the [I;Q] accumulations.

Given the relationship between $\hat{\boldsymbol{r}}_{0opt}^{n}$ estimation accuracy and the ability to remove the carrier-phase effects of multipath, the results of this subsection present a mixed message about the efficacy of this paper's system to estimate and remove the effects of multipath. In the relatively benign multipath environment of the Rhodes Hall roof, solution of the problem in Eqs. (25a)-(25e) with multipath included tends to improve the effective measurement of the direct-path carrier phase. In the high multipath environment in front of Rhodes Hall, however, the algorithm appears to have failed to improve its implicit estimates of the direct-path carrier phase.

D. Analysis of Detrended Wideband Pseudorange After Removal of Multipath Effects

The present subsection analyzes wideband pseudorange, as determined using a type of DLL discriminator and the measured [I;Q] accumulations at a set of code offsets η. In one scenario, the raw [I;Q] measurements are used. In a second scenario, multipath-corrected versions of the [I;Q] measurements are used. If the multipath estimation algorithm of Section III is effective, then these corrected measurements should produce a much smoother wideband pseudorange measurement during the large multipath variations that occur during the $\boldsymbol{r}_a(t)$ antenna motion profiles.

The correction of the raw [I;Q] accumulation measurements for multipath effects proceeds as follows: First, the multipath estimation algorithm of Section III is used to solve the problem in Eqs. (25a)-(25b). Second the X_{dopt} and Y_{dopt} direct-path phasor components in the resulting $\boldsymbol{x}_{opt}$ solution vector are replaced by zero values to produce the vector $\boldsymbol{x}_{opt0X0Y}$. Lastly, this vector is substituted into the accumulations measurement functions in Eqs. (19a) and (19b) and the results are subtracted from the raw accumulation measurement vectors $\boldsymbol{z}_{Ik}$ and $\boldsymbol{z}_{Qk}$ in order to produce the multipath-corrected versions of these vectors:

$$\boldsymbol{z}_{Ikmpcorr} = \boldsymbol{z}_{Ik} - \boldsymbol{h}_I[\boldsymbol{x}_{opt0X0Y}; \bar{\tau}_k, \boldsymbol{r}_a(\bar{\tau}_k)] \tag{32a}$$

$$\boldsymbol{z}_{Qkmpcorr} = \boldsymbol{z}_{Qk} - \boldsymbol{h}_Q[\boldsymbol{x}_{opt0X0Y}; \bar{\tau}_k, \boldsymbol{r}_a(\bar{\tau}_k)] \tag{32b}$$

The discriminator used in this analysis is based on solving a greatly simplified version of the optimization problem in Eqs. (25a)-(25e). This version considers only one sample at a time, and optimizes only the three direct-path parameters $\Delta\tau_d$, X_d, and Y_d. The optimization assumes $M = 0$ multipath components, and it assumes that $\Delta\omega_{nom} = 0$, $\Delta\gamma_{nom} = 0$, $\hat{\boldsymbol{r}}_0 = [1;0;0]$, and $\boldsymbol{r}_a(\bar{\tau}_k) = 0$. In the uncorrected case, the raw $[I;Q]$ accumulation vectors $\mathbf{z}_{Ik}$ and $\mathbf{z}_{Qk}$ are used in the single-sample cost function definition. If multipath corrections are being applied, then $\mathbf{z}_{Ik}$ and $\mathbf{z}_{Qk}$ are replaced by $\mathbf{z}_{Ikmpcorr}$ and $\mathbf{z}_{Qkmpcorr}$ in the cost function.

The optimal estimate of $\Delta\tau_d$ at sample k is designated as $\Delta\tau_{dk}$. It is subtracted from $\bar{\tau}_k$ in order to produce the wide-band DLL estimate of the arrival time of the PRN code, $\bar{\tau}_k - \Delta\tau_{dk}$. This arrival time can be used to compute a wideband accumulated delta pseudorange time history as follows:

$$dP_k = c\sum_{i=2}^{k}\Big[(\bar{\tau}_i - \Delta\tau_{di}) - (\bar{\tau}_{i-1} - \Delta\tau_{di-1}) - \\ - 0.001 round\{1000[(\bar{\tau}_i - \Delta\tau_{di}) - (\bar{\tau}_{i-1} - \Delta\tau_{di-1})]\}\Big] \tag{33}$$

This formula is based on the assumption that the accumulation intervals span an integer number of 0.001 sec C/A code periods and thus, that their nominal differential transmission times, are exactly integer multiples of 0.001 sec.

Detrended versions of the results from the Eq.-(33) calculation are plotted in Fig. 12. These results are for PRN 32 during the second antenna motion sequence that was run in front of Rhodes Hall. Thus, they correspond to the case that produced the amplitude results shown in Fig. 10. The red dots in Fig. 12 are based on the raw $[I;Q]$ accumulations. The blue dots correspond to multipath-corrected accumulations, with the multipath corrections coming from the $M = 4$ component case that was solved for this data set. Thus, the blue dots in Fig. 12 correspond to the dashed magenta curve in Fig. 10. Also plotted in Fig. 12 is the accumulated beat carrier phase as computed without the extra DLL calculations -- the green dots. They correspond to a modified version of the Eq.-(33) calculation that omits the $\Delta\tau_{di}$ and $\Delta\tau_{di-1}$ terms. This case has been plotted for reference purposes. Note that the curves in $\Delta\tau_{di}$ have been detrended using a common quadratic detrending polynomial in order to clearly show the pseudorange changes.

It is clear from Fig. 12 that the multipath corrections improve the DLL discriminator performance. The uncorrected wide-band pseudorange, the red dots, shows large variations that correlate well with the large multipath-induced amplitude variations seen in Fig. 10. The multipath-correct blue dots show much less influence from the multipath effects. Their peak excursion is only 19.6 m, as opposed to 36.8 m for the uncorrected discriminator, and their RMS excursions are only 6.2 m, down from 10.4 m for the uncorrected pseudorange. It is interesting to note how the green DLL curve seems to be following the red dots, but with an attenuated amplitude. This is likely the effect of the carrier-aiding of the DLL coupled with its limited direct DLL feedback bandwidth.

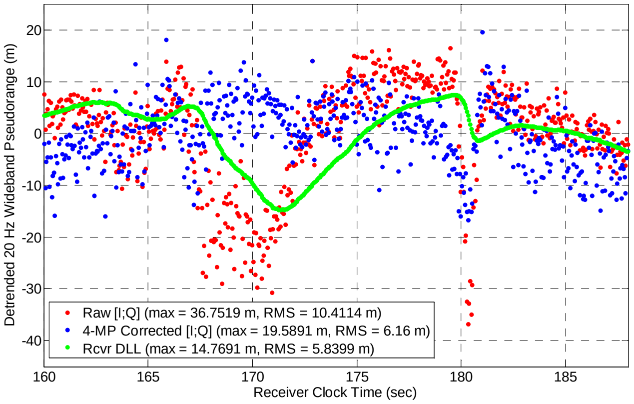

Fig. 12 Detrended pseudorange time histories for uncorrected (red), multipath-corrected (blue) and software receiver DLL (green) for PRN 32 and antenna motion system operating in front of Rhodes Hall.

The results of Fig. 12 are encouraging. Unfortunately, they are not the rule. Thirteen additional cases have been analyzed using this same technique. The dramatic DLL discriminator improvement caused by the multipath corrections was repeated in only one of these other cases. In most of the cases the uncorrected and multipath-corrected DLL discriminators performed about the same, although the multipath discriminator was often slightly better in terms of RMS and peak error. In a few cases the multipath-corrected discriminator had slightly poorer performance, and in one case it had distinctly poorer performance. Note, however, that the two cases with significantly improved performance were the cases with the poorest original uncorrected performance. Therefore, the multipath corrected discriminator may provide a good means of limiting worst-case multipath errors.

VI. SUMMARY AND CONCLUSIONS

This paper has developed and presented a method to estimate the multipath in received GNSS signals and to separate out its effects from the direct-path signal in order to better track the code and carrier of the direct signal. The method works by considering the amplitude and phase variations of in-phase and quadrature accumulations at multiple code delay offsets and their response to a known antenna motion profile. This approach constitutes an enhanced version of the Multipath Estimating Delay-Lock Loop that might better be described as a Multipath Estimating combined Phase-Lock Loop/Delay-Lock Loop. It includes a model of the antenna motion effects on the receiver accumulations, and it estimates the code delays, carrier phases, carrier amplitudes, and directions of arrival of the direct and multipath signal components. The estimation of these quantities is carried out using a weighted nonlinear batch least squares algorithm. A prototype implementation operates on an entire time series of data as a single data batch. The batch estimator has been demonstrated to have a mathematically observable parameter vector.

The new technique has been tested using data from an antenna motion system that undergoes 0.10 m excursions on 3 independent axes over a period of 25 sec. The method demonstrated an ability to fit the carrier-amplitude variations that are caused by multipath. It improved direct-signal carrier phase data when operating in a relatively benign multipath environment. It also improved direct-signal wideband pseudorange when operating in a multipath environment that strongly degrades pseudorange discriminator performance.

ACKNOWLEDGEMENTS

The authors were helped by Cornell's "Urban Wind" project team, undergraduates Rogerio Bonatti, Ryan Gryszko, and Mikhail Yakhnis. They provided and operated the antenna motion system used to generate experimental results. Prof. Ephrahim Garcia is their faculty advisor.

REFERENCES

[1] Van Nee, R.D.J., Siereveld. J., Fenton, P.C., and Townsend, B.R., "The Multipath Estimating Delay Lock Loop Approaching Theoretical Accuracy Limits," *Proc. IEEE Position, Location, and Navigation Symp.*, Las Vegas, Nevada, April 1994.

[2] Townsend, B.R., and Fenton, P.C., "A Practical Approach to the Reduction of Pseudorange Multipath Errors in a L1 GPS Receiver," *Proc. ION GPS 1994*, Salt lake City, Utah, Sept. 1994.

[3] Townsend, B.R., Fenton, P.C., Van Dierendonck, K.J., and Van Nee, D.J., "Performance Evaluation of the Multipath Estimating Delay Lock Loop," *Navigation*, Vol. 42, No. 3, Fall 1995, pp. 503-514.

[4] Braasch, M.S., "Multipath Effects," in *Global Positioning System: Theory and Applications, Vol. I*, Parkinson, B.W. and Spilker, J.J. Jr., eds., American Institute of Aeronautics and Astronautics, (Washington, 1996), pp. 547-568.

[5] Van Dierendonck, A.J., "Mathematics of Multipath Distortion," PowerPoint Presentation, available online at http://www.ima.umn.edu/talks/workshops/8-16-18.2000/van-dierendonck/Multipath.PDF , April 2000.

[6] Townsend, B., Wiebe, J., and Jakab, A., "Results and Analysis of Using the MEDLL Receiver as a Multipath Meter," *Proc. ION National Technical Meeting*, Anaheim, CA, Jan. 26-29, 2000.

[7] Psiaki, M.L., and O'Hanlon, B.W., "System Identification of a GNSS Receiver's RF Filter Impulse Response Function," *Proc. ION GNSS 2011*, Portland, OR, Sept. 20-23, 2011, pp. 3690-3708.

[8] Gill, P.E., Murray, W., and Wright, M.H., *Practical Optimization*, Academic Press, (New York, 1981), pp. 39-40, 105-107, 113-115, 167-169.

[9] Fletcher, R., *Practical Methods of Optimization*, J. Wiley & Sons, (New York, 1987), pp. 24-26, 95-107, 159-162.

[10] Psiaki, M.L., and Hinks, J.C., "Numerical Solution of a Generalized Wahba Problem for a Spinning Spacecraft," *Journal of Guidance, Control, and Dynamics*, Vol. 35, No. 3, May-June 2012, pp. 764-773.

[11] Bar-Shalom, Y., Li, X.-R., and Kirubarajan, T., *Estimation with Applications to Tracking and Navigation*, J. Wiley & Sons, (New York, 2001), pp. 109-113.

[12] Wahba, G., "A Least Squares Estimate of Satellite Attitude," *SIAM Review*, Vol. 7, No. 3, 1965, p. 409.

[13] Wertz, J.R., ed., *Spacecraft Attitude Determination and Control*, D. Reidel Pub. Co., (Boston, 1978), pp. 426-428.